A NUMERICAL MODEL FOR NON-LINEAR COUPLED ANALYSIS OF SEISMIC RESPONSE OF LIQUEFIABLE SOILS

Giuseppe Tropeano[a], Anna Chiaradonna[b,*], Anna d'Onofrio[b], Francesco Silvestri[b]

[a] Department of Civil, Environmental Engineering and Architecture, University of Cagliari, Piazza d'Armi, 09123, Cagliari, Italy

[b] Department of Civil, Architectural and Environmental Engineering, University of Napoli Federico II, via Claudio 21, 80125, Naples, Italy

[*] Corresponding author. Phone: +39 081 768 5916; Cell: +39 329 889 5065.

Email addresses: giuseppe.tropeano@unica.it (G. Tropeano), anna.chiaradonna@unina.it (A. Chiaradonna), donofrio@unina.it (A. d'Onofrio), francesco.silvestri@unina.it (F. Silvestri).

ABSTRACT

A simplified model, able to reproduce the pore pressure build-up until liquefaction under seismic shear loads, has been implemented in a one-dimensional code for loosely coupled site response analysis in effective stress. One-dimensional consolidation relationships have been also integrated in the formulation in order to simulate both generation and dissipation of excess pore water pressure. The performances of the code are evaluated by analysing an ideal soil profile, a centrifuge model test and an instrumented test site. The comparison between records and simulations highlighted that, notwithstanding the simplicity of the proposed approach, the code provides reliable predictions.

Keywords: (loosely coupled) effective stress analysis, liquefaction, pore water pressure, dissipation, centrifuge, test site.

1. Introduction

Seismic strong-motion events occurred during past years, such as the 2015 Gorkha (Nepal), the 2012 Emilia (Italy), the 2010-2011 Canterbury (New Zealand) and the 2011 Tohoku-Oki (Japan) earthquakes, demonstrated that coupled phenomena in sandy/silty soils cannot be neglected in the analysis of site response; nevertheless, this issue is still a demanding task for the design of infrastructures and facilities.

The soil response of saturated soils under strong motion seismic loading is ruled by rather complex mechanical processes, which may be basically ascribed to hysteretic behaviour and volumetric-distortional coupling. The first consists in a decrease of the shear modulus associated with an increase in energy dissipation (damping); the second is related to plastic irreversible straining, that takes place at high shear loads and induces either volumetric strains in drained conditions, or pore pressure changes in undrained conditions. This latter may evolve into liquefaction in loose sandy soils.

While the importance of first class of non-linear effects has been widely recognized [1], [2] and modelled in the most common and/or commercial codes performing seismic site response [3]–[6], the modelling of volumetric/distortional coupling still remains a challenging issue, due to the limitations of simplified approaches and to the specific expertise required for calibrating advanced constitutive models.

In this study, a simplified pore water pressure model was implemented in a 1D computer code in order to carry out effective stress analyses. A so-called ‘loosely coupled approach’ [7] was followed taking into account the stiffness and strength degradation of the soil due to progressive build-up of pore water pressures induced by cyclic shear loading. Redistribution and dissipation of excess pore pressure during and after the seismic event are also considered, according to the one-dimensional consolidation theory [8].

The numerical model can represent a useful tool for engineering practice, since it requires only few parameters, clearly defined and easy to be calibrated.

The description of the numerical code is briefly presented in Section 2, while the implementation of the constitutive relationships is detailed in Section 3.

The overall performance of the numerical model was first evaluated on ideal soil profiles (section 4) and then validated by simulating a centrifuge test and seismic events recorded on well-instrumented test site (section 5).

2. Numerical code

SCOSSA is a computer code for one-dimensional (1D) seismic response analysis [9]; it models a soil profile as a system of consistent lumped masses, connected by viscous dampers and springs with hysteretic non-linear behaviour (Fig. 1a,b).

The discretization of the subsoil profile into the lumped parameter system is based on Kuhlemeyer and Lysmer [10] criterion, where the maximum sub-layer thickness is a suitable fraction (1/6 - 1/8) of the minimum wavelength to be transmitted.

Currently, the code is able to simulate both the transient seismic response ('stick' mode) and the permanent deformation mechanisms ('slip' mode) accounting for the coupled effects of deformability and strength [9] by carrying out total stress analyses.

The performances of the code in the 'stick' mode [9], were verified and validated together with those of other codes during an international benchmark within the framework of PRENOLIN project [1], [2].

For the purposes of this paper, only the 'stick' mode is handled, since a simplified pore water pressure model is here implemented into the code in order to model the transient seismic site response at large shear strains.

The code SCOSSA performs non-linear seismic response analyses solving the ground motion equations in the time domain. The seismic response in terms of absolute displacements, **d**, to a base ground motion, a_g (Fig. 1), can be computed by integrating the following system:

$$\mathbf{M}\,\mathbf{a} + \mathbf{C}\,\mathbf{v} + \mathbf{K}\,\mathbf{d} = \mathbf{f} \qquad (1)$$

where **M**, **C** and **K** are the mass, damping and stiffness matrices respectively, **f** is the vector of applied forces. This latter depends on the input accelerogram, $\ddot{v}_g$, which can be applied as 'within' or 'outcrop' motion at the bedrock [9].

The elements of the **M** and **K** matrices are defined from the mass, m_j, and the current spring stiffness, k_j, of a generic layer j, as follows:

$$m_1 = \frac{\rho_1 h_1}{2}; \quad m_j = \frac{\rho_j h_j + \rho_{j-1} h_{j-1}}{2}; \quad m_{n+1} = \frac{\rho_n h_n}{2}; \tag{2}$$

$$k_j = \frac{G_j}{h_j} \tag{3}$$

where ρ_j, h_j, and G_j are the density, thickness and tangent shear modulus of the j-th layer, respectively.

The viscous damping matrix, **C**, is defined according to the full Rayleigh damping formulation [11]:

$$\mathbf{C} = \alpha_R \mathbf{M} + \beta_R \mathbf{K} \tag{4}$$

where the constants α_R and β_R are set as functions of the minimum soil damping ratio, ξ_{min}, the fundamental frequency of the subsoil profile and the predominant frequency of the input motion.

Modifications to the basic numerical procedure of the code have been required for implementing the pore pressure generation and dissipation models. The flowchart in Fig. 2 resumes the schematic algorithm adopted in the upgraded code for each time step.

New additional routines have been introduced in the original algorithm implemented in SCOSSA, i.e. consolidation, generation of pore water pressure and adjustment of the shear modulus (shaded boxes in Fig. 2). A detailed description of these latter routines will be provided in the following section 3.

Following the flowchart of Fig. 2, an initial updating of the vector of input forces, **f**, is carried out for the i-th time step. During the same time interval, a new distribution of the pore water pressure along the soil profile is evaluated starting from that evaluated at the previous time instant, assuming a constant value of the consolidation coefficient, c_v (see § 3.2). The consolidation phenomenon

causes a reduction of the excess pore water pressure, with a negative variation of the pore pressure ratio, r_u; this latter is defined as the ratio between the pore pressure, Δu, and the initial effective stress of the soil, σ'_0.

At the same time step increment, the code uses the Newmark β method [12] to numerically integrate the equations of motion:

$$\begin{cases} \mathbf{M}\,\mathbf{a}_{i+1} + \mathbf{C}\,\mathbf{v}_{i+1} + \mathbf{K}\,\mathbf{d}_{i+1} = \mathbf{f}_{i+1} \\ \mathbf{v}_{i+1} = \mathbf{v}_i + \Delta t\,(1-\gamma_N)\,\mathbf{a}_i + \Delta t\,\gamma_N\,\mathbf{a}_{i+1} \\ \mathbf{d}_{i+1} = \mathbf{d}_i + \Delta t\,\mathbf{v}_i + \Delta t^2\,(1/2-\beta_N)\,\mathbf{a}_i + \Delta t^2\,\beta_N\,\mathbf{a}_{i+1} \end{cases} \tag{5}$$

The default coefficients are set equal to $\gamma_N = 0.5$ e $\beta_N = 0.25$, so that the method is unconditionally stable and no numerical damping is introduced.

For a model with n degrees of freedom, the system (5) can be easily solved if expressed in the form:

$$\mathbf{A}\,\mathbf{x}_{i+1} = \mathbf{B}\,\mathbf{x}_i + \mathbf{q}_{i+1} \tag{6}$$

where $\mathbf{x}$ is the vector of the unknown variables:

$$\mathbf{x} = \{\mathbf{a}^T \quad \mathbf{v}^T \quad \mathbf{d}^T\}^T \tag{7}$$

In equation (6), $\mathbf{q}$ is the vector of the external forces, where the first n elements are equal to $\mathbf{f}$, and the remaining $2n$ elements are null; $\mathbf{A}$ and $\mathbf{B}$ are the matrices of the integration method, defined as:

$$\mathbf{A} = \begin{bmatrix} \mathbf{M} & \mathbf{C} & \mathbf{K} \\ -\Delta t\,\gamma_N\,\mathbf{I} & \mathbf{I} & \mathbf{0} \\ -\Delta t^2\,\beta_N\,\mathbf{I} & \mathbf{0} & \mathbf{I} \end{bmatrix}; \quad \mathbf{B} = \begin{bmatrix} \mathbf{0} & \mathbf{0} & \mathbf{0} \\ \Delta t\,(1-\gamma_N)\,\mathbf{I} & \mathbf{I} & \mathbf{0} \\ \Delta t\,(1/2-\beta_N)\,\mathbf{I} & \Delta t\,\mathbf{I} & \mathbf{I} \end{bmatrix} \tag{8}$$

where $\mathbf{I}$ and $\mathbf{0}$ are the unit and null matrix, respectively, with $n \times n$ dimension.

The numerical solution of system (6) is reduced to the inversion of the $3n \times 3n$ matrix $\mathbf{A}$ for each time step, which can be carried out by adopting exact or iterative methods. The code uses an exact inversion method based on the Crout-Doolittle factorization algorithm, modified for band matrices. Since the variability of the stiffness matrix, $\mathbf{K}$, also depends on the solution of the system (5), as a first attempt the stiffness matrix is set equal to that calculated at the previous instant.

The solution of the system (5) leads to the computation of the kinematic variables, i.e. acceleration, velocity and displacement. Then, the shear strain increment, $\Delta\gamma_j$, is obtained through:

$$\Delta\gamma_j = \frac{\Delta d_j - \Delta d_{j+1}}{h_j} \tag{9}$$

where $\Delta d_j = d_j^{\,i+1} - d_j^{\,i}$ is the displacement variation in the time interval Δt, while h_j is the sub-layer thickness.

A continuous stress-strain relationship is used to compute the shear stress increment, $\Delta\tau_j$, in the time interval Δt, as a function of the shear strain level (eq. 9) and of the pore pressure ratio, r_u, defined in the previous time instant (through the constitutive model described in § 3).

The variation of shear stress generates accumulation of excess pore water pressure, that is computed using a simplified stress-based model for prediction of pore pressure build-up (see § 3.1). Finally, the effective increment of excess pore pressure ratio is calculated as balance between the generated and dissipated excess pore pressure (see § 3.2).

The resulting value of r_u is used to update the constitutive relationship and computing a new value of the tangent shear modulus, G (see § 3).

The current value of the stiffness for the j-th sub-layer, k_j, is computed by the tangent shear modulus, G_j, as follows:

$$k_j = \frac{G_j(\gamma_j)}{h_j} \tag{10}$$

Through equation (10), it is possible to define the stiffness matrix from the current shear strain level and excess pore pressure ratio, r_u.

Due to the mutual dependency between $\mathbf{K}$ and the system solution, $\mathbf{x}$, an iterative computation needs to be applied at each time step. As a first attempt, the stiffness matrix is set equal to that calculated at the previous instant, i.e. $[\mathbf{K}^{i+1}]_{k=0}=\mathbf{K}^i$; The system is solved and the strain, $[\boldsymbol{\gamma}^{i+1}]_{k=0}$, and stress, $[\boldsymbol{\tau}^{i+1}]_{k=0}$, vectors are calculated, by which the stiffness matrix of the layering is again evaluated as $[\mathbf{K}^{i+1}]_{k=1}$. The procedure is iterated until the maximum value of the relative error, ε_{rel}, between two subsequent solutions, $[\mathbf{x}^{i+1}]_{k-1}$ and $[\mathbf{x}^{i+1}]_k$, defined as:

$$\varepsilon_{rel} = \max\left\{\frac{\left|\left[x_j\right]_k^{i+1} - \left[x_j\right]_{k-1}^{i+1}\right|}{10^{-6} + \left|\left[x_j\right]_k^{i+1}\right|}\right\} \qquad \text{with } j = 1, 2, ..., n \text{ (layer index)} \tag{11}$$

is less than a fixed tolerance value, ε_{tol}. This iterative solution reduces the numerical instability occurring at the reversal points in the hysteresis loop.

3. Constitutive model

The effective-stress site response analysis is carried out following a "loosely coupled" approach where a soil constitutive model in total stress (§ 3.1) is adopted in combination with a semi-empirical model for the prediction of pore pressure build-up (§ 3.2) and dissipation (§ 3.3).

3.1. Cyclic stress-strain behaviour

The non-linear hysteretic response of the springs is modelled using the "Modified Kondner and Zelasko" (MKZ) [13] relationship, along with extended Masing rules [14]. The stress-strain relationship (i.e. the backbone curve) for a monotonic loading path in simple shear is given by:

$$F_{bb}(\gamma) = \frac{\delta_G G_0 \gamma}{1 + \beta\left(\frac{\gamma}{\gamma_r}\frac{\delta_G}{\delta_\tau}\right)^{s'}} \tag{12}$$

where γ is the shear strain level, G_0 is the initial shear modulus, γ_r is the reference shear strain, β and s' are two dimensionless factors and δ_τ and δ_G are two degradation index functions. The modulus degradation index function, δ_G, is defined as:

$$\delta_G = \sqrt{1 - r_u} \tag{13}$$

while the corresponding stress degradation index function, δ_τ, is given by:

$$\delta_\tau = 1 - r_u^{\mu} \tag{14}$$

where μ is an exponential constant which expresses the sensitivity of the backbone curve to pore water pressure changes. Matasovic and Vucetic [15] defined the constant μ on the stress-strain response obtained from strain-controlled cyclic simple shear tests on Californian sandy soils. They found μ values ranging between 3.5 and 5.

The same direct relationship between shear modulus and excess pore water pressure is also frequently used in other codes suitable for effective stress analyses codes (e.g. DESRA-2 [16]; D-MOD2000 [17]).

Unlike the second rule of the original Masing criteria, the formulation by Phillips and Hashash [18] is adopted for expressing the stress-strain relationship in unloading-reloading conditions. Introducing the degradation indexes, the relationship proposed by Moreno-Torres et al. [19] is obtained:

$$F_{ur}(\gamma) = F^*(\gamma_m)\left[\frac{G_0\,\delta_G\,(\gamma-\gamma_c)}{1+\beta\left(\frac{\delta_G}{\delta_\tau}\right)^{s'}\left(\frac{\gamma-\gamma_c}{2\gamma_r}\right)^{s'}} - \frac{G_0\,\delta_G\,(\gamma-\gamma_c)}{1+\beta\left(\frac{\delta_G}{\delta_\tau}\right)^{s'}\left(\frac{\gamma_m}{\gamma_r}\right)^{s'}}\right] + \frac{G_0\,\delta_G\,(\gamma-\gamma_c)}{1+\beta\left(\frac{\delta_G}{\delta_\tau}\right)^{s'}\left(\frac{\gamma_m}{\gamma_r}\right)^{s'}} + \tau_c \quad (15)$$

In equation (15), γ_c and τ_c are, respectively, the reversal shear strain and shear stress, γ_m is the maximum shear strain attained during the time history, and $F^*(\gamma_m)$ is a damping reduction factor, defined as follows:

$$F^*(\gamma_m) \doteq \frac{\xi_{\exp}(\gamma)}{\xi_{Mas}(\gamma)} = p_1 - p_2\left(1-\frac{G(\gamma_m)}{G_0}\right)^{p_3} \quad (16)$$

In equation (16), p_1, p_2 and p_3 are non-dimensional parameters obtained from the best fit of the ratio between the strain-dependent hysteretic damping measured in laboratory tests, $\xi_{\exp}(\gamma)$, and that calculated using the conventional Masing rules, $\xi_{\mathrm{Mas}}(\gamma)$; $G(\gamma_m)$ is the secant modulus corresponding to the maximum shear strain γ_m attained during the loading history (see Phillips and Hashash [18], for details). The updated formulation modifies the Masing unloading-reloading rules, providing a better agreement with the experimental damping-strain curves for large shear strains.

Fig. 3a shows the predicted effect of pore pressure build up on stress-strain cycles: the shear modulus reduction curve is updated every time an excess pore pressure change occurs (Fig. 3b). Stress-strain cycles computed adopting a total stress analysis are reported for comparison, clearly showing an overall higher shear modulus.

Neglecting the excess pore water pressure, equations (12) and (15) are reduced to the original formulation in total stress described by Tropeano et al. [9].

The parameters of the shear modulus reduction curve (equation 12), i.e. γ_r, β and s', are fitted on the cyclic laboratory test results through non-linear multi-regression of the experimental data points. Nevertheless, cyclic laboratory tests often are not driven to failure and, consequently, the G/G_0 curve reproduced by the model is well-constrained by the data at small to moderate shear strains but does not necessarily provide an accurate representation of soil strength at large shear strains. Such inaccuracy may result in significant errors for seismic response analyses involving shear stress levels near failure condition [20].

Several researchers have proposed different adjustment procedures of the G/G_0 curve ([21]–[23]) in order to solve the problem. In this study, the experimental data were fitted through the interpolation method suggested by Gingery and Elgamal [20], which provides a hyperbolic-like curve as a smooth transition between moderate strain levels and failure. As a results, the $\tau : \gamma$ relationship simultaneously matches the behaviour observed at small to moderate strains and the shear strength of the soil at large strains.

This interpolation procedure scales equation (12) using a raised cosine function to force the backbone curve to predict the correct shear strength by intercepting a given G/G_0 value at a defined shear strain value (i.e. the supposed failure strain).

The value of shear strength, τ_{ff}, depends on the initial stress state in the soil and on the way the shear stress is applied. As reported by Hardin and Drnevich [24], for initial geostatic stress conditions and shear stress applied to horizontal and vertical planes, $\tau_{ff,}$ can be calculates as follows:

$$\tau_{ff} = \left[\left(\frac{1+K_0}{2} \sigma'_v \sin\varphi' + c' \cos\varphi' \right)^2 - \left(\frac{1-K_0}{2} \sigma'_v \right)^2 \right]^{1/2} \quad (17)$$

where K_0 is the coefficient of earth pressure at rest; σ'_v is the vertical effective stress and c' and φ' are the strength parameters in terms of effective stress. Hardin and Drnevich [24] specified that effective stress conditions are used in equation (17) even though undrained conditions occur in dynamic loading.

The modified G/G_0 curve is interpreted again with the MKZ relationship. In this way, the resulting parameters, γ_r, β and s', are both representative of the best-fitting on the available laboratory data and respectful of the shear strength of the soil.

Fig. 4 shows an application of the described procedure: the experimental data from laboratory tests on a silty sand [25] (Fig. 4a) were fitted to predict the stress-strain curve up to failure at 5, 15 and 25 m depth from the ground level along a soil profile characterised by constant shear wave velocity (Fig. 4b).

The above mentioned constitutive model is updated at every time step as function of the current value of the pore pressure ratio, r_u. This latter is computed through the simplified stress-based model proposed by Chiaradonna et al. [26]. The model has also been generalized in order to simulate both accumulation and dissipation of excess pore water pressure during the shaking and the post-seismic phases.

3.2. Generation of excess pore water pressure

The pore pressure build-up can be computed by a simplified model by adopting an endochronic-based damage parameter, κ, which permits avoiding the use of empirical criteria to convert the irregular shear loading into an equivalent number of cycles [26].

The model is based on simple analytical relationships, and allows for a straightforward calibration of the parameters on the results of cyclic laboratory tests. From these latter, the number of cycles at liquefaction, N_L, is univocally related through the cyclic resistance curve to the cyclic resistance ratio, *CRR*, between the peak shear stress amplitude and the initial effective stress. The cyclic resistance curve is analytically described by the following equation:

$$\frac{\left(CRR - CSR_t\right)}{\left(CSR_r - CSR_t\right)} = \left(\frac{N_r}{N_L}\right)^{\frac{1}{\alpha}} \tag{18}$$

where (N_r, CSR_r) is a reference point, CSR_t the asymptotic value of *CRR* as the number of cycles tends to infinite, and α is the slope of the best-fit relationship in a log-log scale (Fig. 5a).

The parameters CSR_t and α are used to compute the damage parameter, κ, for any loading pattern. For a regular harmonic loading of given amplitude, *CSR*, i.e. the ratio between the modulus of the maximum shear stress, $|\tau_{max}|$, and the initial effective stress, κ is proportional to the number of cycles, *N*, and it can be written as [26]:

$$\kappa = 4N\left(CSR - CSR_t\right)^{\alpha} \tag{19}$$

Combining equations (18) and (19), the damage parameter at liquefaction, κ_L, can be expressed as follows:

$$\kappa_L = 4\,N_r\left(CSR_r - CSR_t\right)^{\alpha} \tag{20}$$

The pore pressure model defines also an univocal relationship between the normalized number of cycles, N/N_L and the pore pressure ratio, r_u with the polynomial function [26]:

$$r_u = a\left(\frac{N}{N_L}\right)^{b} + (0.95 - a)\left(\frac{N}{N_L}\right)^{d} \tag{21}$$

where *a*, *b*, *c* and *d* are curve-fitting parameters (Fig. 5b). Given the proportionality between the number of cycles, *N*, and the damage parameter, κ (eq. 19), any pore pressure change can be expressed as a variation of the normalized damage parameter, κ/κ_L (see [26] for details).

For an irregular shear loading history, expressed as follows:

$$\tau^*(t) = \frac{|\tau(t)|}{\sigma_0'} \tag{22}$$

the damage parameter, κ, can be computed at every time instant as:

$$\kappa(t) = \kappa_0 + d\kappa \tag{23}$$

where κ_0 is the damage cumulated at the last reversal point of the function (τ^*- CSR_t) reached at the time instant *t*. The parameter κ_0 can be defined as follows:

$$\kappa_0 = \begin{cases} \kappa(t-dt) & \text{if } \dot{\tau}^*(t) = 0 \quad \text{or } \tau^*(t) = CSR_t \\ \kappa_0(t-dt) & \text{if } \dot{\tau}^*(t) \neq 0 \quad \text{or } \tau^*(t) \neq CSR_t \end{cases} \tag{24}$$

i.e. κ_0 is a stepwise function assuming the value of the damage parameter gained at the time step ($t - dt$) every time the stress ratio reaches a local maximum value or when $\tau^* = CSR_t$.

The increment of the damage parameter, $d\kappa$, in the time interval dt is given by:

$$d\kappa = \begin{cases} 0 & \text{if } \tau^*(t) < CSR_t \\ \left[\tau_0^*(t) - \tau(t)\right]^{\alpha} & \text{if } \tau^*(t) \geq CSR_t \end{cases} \quad (25)$$

where $\tau_0^* = \tau_{\max}^*$ if $\dot{\tau}^*(t) < 0$ and $\tau_0^* = CSR_t$ otherwise.

The damage function increases when τ^* overcomes CSR_t, which represents the threshold below which there is no pore pressure build-up [26].

In the discrete time-step analysis, it is possible to define the "generated damage" increment, $\Delta\kappa_{gen}$, as follows:

$$\Delta\kappa_{gen} = \kappa_{i+1} - \kappa_i \quad (26)$$

3.3. Dissipation of excess pore water pressure

The dissipation of excess pore water pressure during a time step is also taken into account, by solving the diffusion equation, also known as Terzaghi 1D consolidation equation [8]:

$$\frac{\partial u}{\partial t} = c_v \frac{\partial^2 u}{\partial z^2} \quad (27)$$

where c_v is the vertical consolidation coefficient, and the pore water pressure, u, is a function of both the depth, z, and the time, t.

For a homogeneous compressible soil layer, the consolidation equation (27) can be rewritten into an explicit finite difference form as [28]:

$$u_{2j-1}^{\,i+1} \approx u_{2j-1}^{\,i} + \beta\left(u_{2j-2} - 2u_{2j-1} + u_{2j}\right)^i \quad (28)$$

where:

$$\beta = c_v \frac{\Delta t}{\Delta z^2} \quad (29)$$

According to equation (28) the pore pressure at time i+1 for a layer j-th can be calculated by knowing the conditions at time i (u_{2j-2}, u_{2j-1} and u_{2j} in Fig. 1c). If a regular depth discretization, Δz,

is adopted, the accuracy of the solution of equation (28) is inversely proportional to the value of Δt and Δz. Furthermore, the solution is numerically stable if $\beta < 0.5$; it is generally assumed a value equal or less than 0.1. The above requirements entail the need to adopt values for Δt and Δz small enough and calibrated on the parameter c_v.

More details about the development and verification of the formulation adopted for consolidation analysis can be found in [29].

In lack of direct measurements, the consolidation coefficient, c_v, of each layer can be computed through its well-known definition:

$$c_v = \frac{k\, E_{oed}}{\gamma_w} \tag{30}$$

By knowing the unit weight of the water, γ_w, the permeability, k, and the oedometric modulus, E_{oed}, of the soil. From the elasticity theory, the oedometric modulus can be related to the stiffness of the soil, G_0, and the Poisson's ratio, ν, as:

$$E_{oed} = \frac{2G_0\left(1-\nu\right)}{\left(1-2\nu\right)} \tag{31}$$

Using equations (28) and (29), it is then possible to define a reduction of excess pore water pressure for every time step and the corresponding decrease of pore pressure ratio, Δr_u.

The corresponding variation, $\Delta\kappa_{diss}$, of the damage parameter can be computed by inverting eq. (21), through replacement of N/N_L with κ/κ_L [26].

Summarizing, at each time step the excess pore pressure can be generated and partly dissipated; this partially drained condition is reflected by the "net damage parameter", κ_n, being:

$$\kappa_n^{\,i+1} = \kappa_n^{\,i} + \Delta\kappa_{gen} - \Delta\kappa_{diss} \tag{32}$$

where $\Delta\kappa_{gen}$ and $\Delta\kappa_{diss}$ are respectively the variations of damage parameter corresponding to the generation and the dissipation of r_u in the same time step, Δt.

Finally, the pore pressure ratio in the considered time step is computed as:

$$r_u = a\left(\frac{\kappa_n}{\kappa_L}\right)^b + c\left(\frac{\kappa_n}{\kappa_L}\right)^d \quad (33)$$

which is a generalization of the original relationship (equation 21) where the damage parameter, κ, is replaced by the net damage, κ_n, defined by equation (32). Indeed, if the consolidation is neglected, κ_n becomes equal to κ and the original formulation of the relationship is obtained.

Fig. 6 shows an example of application of the pore pressure model in totally undrained and partially drained conditions in the case of a saw-tooth periodic time history of shear stress (Fig. 6a). The damage parameter and pore pressure ratio were computed through the cyclic resistance curve and the pore pressure relationship plotted in Figs. 5a,b.

As a result of the application of eqs. (23), (24) and (25), in totally undrained conditions, the damage parameter increases when τ^* exceeds the threshold value, CSR_t; otherwise, it remains constant. Conversely, in partially drained conditions, the accumulation of the net damage parameter is slower and it decreases after the end of shaking (Fig. 6b). The same trend can be observed also in the time history of the normalized damage parameter (Fig. 6c).

Once the pore pressure ratio is expressed as a function of the net damage parameter by equation (33), the time history of excess pore water pressure (Fig. 6d) can be calculated, whatever the drainage conditions.

After the end of the shear loading, the model clearly simulates the consolidation process.

It must be remarked that the liquefaction condition is assumed to occur for r_u equal to 95%, according to a stress-based criterion. This assumption also avoids computational problems, which would be otherwise induced on the stiffness matrix by the zeroing of the effective stresses if liquefaction occurs.

4. Performance on ideal soil profiles

The performance of the SCOSSA-PWP code was preliminarily verified adopting a simple scheme of a uniform 30 m thick layer of silty sand (Fig. 7), with the ground water table located at 1 m depth.

The selected reference input motion is the NS component of the main-shock of Umbria-Marche seismic sequence (26/09/1997, M_w = 6), recorded at the Assisi station with a maximum acceleration of 0.273 g (ASS, Fig. 7c). The time history of acceleration was applied as an outcrop motion at the bedrock, which was modelled as a permeable visco-elastic half-space with the properties reported in Table 1.

The same table also shows the main properties of the silty sand.

Figs. 7a,b show the profiles of the shear wave velocity, V_S, and the shear strength, τ_{ff}, respectively. The profile of V_S corresponds to a a power function of z with an exponent equal to 0.25 characterised by a value of 100 m/s at surface (Fig. 7a). The shear strength was computed according to equation (17), but the profile was discretized into a stepwise-function for sake of simplicity (blue line in Fig. 7b).

The non-linear and dissipative behaviour of the soil was modelled adopting the curves plotted in Fig. 7d, which result from the application of the MKZ model to the experimental data adjusted following the procedure described in Section 3.

The characterisation of cyclic strength of the silty sand (see eq. 18 and Fig. 5a) was based on the experimental data reported by Porcino and Diano [27]. The same data from cyclic simple shear tests were also used to calibrate the pore pressure model (eq. 21 and Fig. 5b). Full details about the calibration procedure can be found in [26].

The degradation parameter of eq. (14), μ, has been set to the mean value of 3.5, as suggested by Matasovic and Vucetic [15], while the consolidation coefficient, c_v, computed through eqs. (30) and (31) by setting $k = 10^{-5}$ m/s and $\nu = 0.3$ was equal to 1.31 m^2/s.

Total (TS) and effective stress (ES) analyses were performed on the soil column. In the effective stress analyses, the calculations were carried out according to the procedure described in section 2 (loosely coupled approach), while in the total stress analyses the pore pressure model was adopted following a decoupled approach. In this latter case the computation followed the original algorithm of SCOSSA [9], and the shear stress history resulting from the total stress analysis was used to

predict the pore pressure build-up induced by the cyclic loading, by applying "offline" the pore water pressure model (§ 3.1).

Fig. 8 shows the results in terms of the profiles of maximum acceleration, shear strain, stress and pore pressure ratio computed by total and effective stress analyses, both considering and neglecting the dissipation of excess pore pressure.

The maximum acceleration computed through the effective stress analyses is lower than that obtained by the total stress analysis along the first 3 m of the soil column and between 9 and 19 m (Fig. 8a).

Higher shear strains are mobilized along the shallowest part of the column in the effective stress analyses, due to the degradation of stiffness induced by excess pore pressure build-up.

Differences between the shear strain profiles computed applying the coupled and decoupled approaches can be better appreciated looking at the shear stress-strain cycles at 3 m depth, reported in Figure 3.

Few differences are found between the maximum shear stress profiles in coupled and decoupled analyses; in this latter case, the stress amplitude are slightly higher because they are less affected by the accumulation of excess pore water pressure.

As a consequence, the pore water pressures computed by the decoupled approach are higher than those obtained by the coupled approach and liquefaction condition is reached in the shallowest 5 m of the soil column (Fig. 8d).

In partially drained conditions, an accurate discretization of the soil profile was required. Indeed, the maximum thickness of each layer should satisfy, at the same time, the Kuhlemeyer and Lysmer [10] criterion and the numerical stability of the consolidation subroutine, $\beta < 0.1$, described in § 3.2:

$$\left(10\, c_v\, \Delta t\right)^{0.5} < \Delta z < \frac{V_S}{6\, f_{\max}} \tag{35}$$

i.e. the discretization of soil column is a function of both soil properties (shear wave velocity, permeability) and input motion features (time step, maximum frequency).

Few differences are found in the maximum acceleration and shear strain profiles computed by considering or neglecting the dissipation process (Fig. 8a,b). The maximum shear stress profiles are identical, highlighting that consolidation process is triggered after the peak stress value is attained (Fig. 8c). This is also confirmed by the maximum pore pressure ratio profiles, which are quite similar in the two analyses, except for the first meters under the ground water table, where the hydraulic gradients is high enough to induce a sensible reduction in excess pore water pressure (Fig. 8d).

Figs. 8e-f-g detail the effect of consolidation on the shear stress and excess pore pressure at 3 m depth. A clear reduction of excess pore pressure is induced by the simultaneous dissipation process (Fig. 8g), showing the importance of a correct evaluation of consolidation characteristics of soil for an appropriate prediction of the seismic response, if an effective stress analysis is carried out taking into account the dissipation process.

5. Validation on a centrifuge test

Comparison with Centrifuge test No. 1 carried out during the VELACS (Verification of Liquefaction Analysis by Centrifuge Studies) project has been considered, since it reproduces a simple one-dimensional scheme in free-field conditions [30].

A horizontal uniform layer of Nevada sand was placed in a laminar box with a relative density of about 40%. Fig. 9 shows the cross section of the laminar box and some of the sensors used in the test. The laminar box consists of 30 rectangular aluminium rings assembled on top of each other with roller bearings in between. The roller bearings allow the box to deform and follow the soil deformations, in order to simulate the response of a semi-infinite sand layer during shaking. The inside dimensions of the laminar box are 45.72 × 20 cm.

The sand layer was fully saturated with water and the total unit weight resulted 19.36 kN/m^3.

The soil was extensively tested in the laboratory in order to properly characterize the static and dynamic behaviour of the material [31].

The model was spun at a centrifuge acceleration of 50 g (hence, the scale factor was n=50), while excited horizontally at the base with the target prototype accelerogram shown in Fig. 10b. The measured vertical acceleration was so small to be considered negligible.

Horizontal (AH) and vertical (AV) accelerometers as well as piezometers (P) allowed for monitoring the soil in terms of horizontal and vertical motions and excess pore pressures, respectively (Figure 9).

The pore pressure time histories measured at the same elevations were essentially identical, verifying the one-dimensional behaviour of the model [30].

In this study, the numerical modelling of the experiment No. 1 was performed in prototype scale, corresponding to a 10 m thick uniform sand layer, with piezometers P1, P2, P3, P4 positioned at 1.45, 2.6, 5 and 7.5 m from the surface, respectively (Fig. 10a).

The groundwater table is at the surface level; the base of the model is considered impervious, while free drainage can occur only through the surface of the sand layer.

The bedrock has been considered as rigid and the horizontal acceleration has been applied as 'inside' input motion at the base of the profile.

The unit weight of sand has been adopted equal to 25.05 kN/m^3 to incorporate the inertia of the rings, as proposed by Taboada [32].

The dynamic properties of Nevada sand were defined based on resonant column test data [31]. Tests were carried out on specimens consolidated at different isotropic pressures, which made it possible to define a power function relating the small-strain stiffness, G_0, to the mean effective stress, p' (Fig. 10c). The obtained relationship plots very close to that suggested for the same sand by Taiebat et al. [33]. From the above G_0-p' relationship, the shear wave velocity profile was obtained as a power function of depth, z (Fig. 10a).

The experimental data from the resonant column tests [31] at p'= 40 and 80 kPa (Fig. 11a) have been considered to define the non-linear and dissipative properties of Nevada sand, again through MKZ model (Fig. 11b).

Figs. 11c,d show the cyclic resistance curve and the pore pressure relationship for Nevada sand, based on the results of cyclic simple shear tests [31]. Differently from the soil considered in the previous example, the Nevada sand exhibits a pore pressure relationship strongly dependent on the cyclic stress ratio applied during the test; indeed, upper and lower bound curves can be defined for fitting the test results, while the pore pressure model requires the definition of a unique $r_u : N/N_L$ relationship. Since the cyclic stress ratio estimated for the reference input motion is higher than 0.3 [34], the upper bound curve has been considered in the analysis.

The degradation parameter, μ, in eq. (15) has been set equal to 3.5.

The consolidation coefficient, c_v was directly back-figured, from a best-fit of the pore pressure dissipation curves recorded at the end of the dynamic shaking. In fact, the proposed model does not necessarily require to assign c_v by separately setting in eq. (30) the values of k and E_{oed}. These latter might be affected by significant uncertainties, if inferred from the laboratory tests on small size specimens and then assigned to the larger centrifuge model, due to likely inhomogeneities of its fabric, density and stress-strain distribution.

Fig. 12 compares the predicted pore pressures versus those measured at the different depths. The left plots focus on the pore pressure response during the shaking, while those to the right show also the subsequent dissipation.

The measured pore pressure trends indicate that soil at P1 and P2 depths definitely liquefied. At P3, the pore pressure ratio reached unity later during the shaking, while at P4 liquefaction did not take place.

All time histories reveal the typical pattern observed in comparable model tests on saturated sand [32], consisting of:

- an initial build-up of excess pore pressure, reaching a plateau in the shallower piezometers as liquefaction took place;
- a dissipation process evolving from the bottom to the top of the layer as the excess pore water is expelled through the surface and the partially or fully liquefied soil densifies.

In the simulation, an excess pore pressure ratio, r_u, equal to 0.95 (liquefaction) is reached after 2 seconds of shaking at the shallow piezometer P1 (1.45 m), as well as at 2.6 m (P2) and 5 m depth (P3). The same simulation well predicts the experimental pore pressure build-up measured at 7.5 m (P4) depth, not exceeding 80% of the effective overburden pressure.

It must be observed that the higher the depth, the earlier the attainment of the maximum pore pressure in the simulation with respect to the experimental results; this can be ascribed to a possible increase with depth of the relative density that is not taken into account in the numerical model (due to the adoption of a unique cyclic resistance curve in the analysis).

Probably the adoption of a constant c_v in the numerical simulation might be the reason why the triggering of dissipation starts at the same instant whatever the depth, i.e. right after the end of the dynamic shaking, whereas in the experimental results the decay of r_u is increasingly delayed approaching surface.

In Fig. 13, the simulated acceleration time histories are compared with the signals recorded at 0, 2.6 and 5.0 m depth. Due to the discretization criterion adopted, while the excess pore pressures were computed exactly at the same depths where piezometers were installed, the accelerations were returned at the top of the corresponding sublayers, i.e. at depths slightly different from those where the horizontal accelerometers were placed.

It can be noted that acceleration amplitudes are overestimated at surface and at 2.6 m depth, particularly after the liquefaction occurrence.

A better prediction is observed at 5.0 m depth: in this case the amplitude of the record are nicely simulated after 5 s.

6. Validation on an instrumented test-site

Another validation benchmark is proposed with reference to a seismic recording array located near to the Sendai port, in the North-East of Japan (Fig. 14a). The recording station, belonging to the PARI network, consists of a surface accelerometer and a downhole geophone at 10.4 m depth. The array is deployed in a Holocene sedimentary soil, called “beach ridge”, consisting of gravel and

sand of marine origin. This surface deposit is underlain by the Pliocene "Geba formation", forming the Northern and Eastern hills and consisting of gravel stone, sandstone, tuff, tufaceous siltstone and lignite [2] and [35].

The Senday array site was selected as a validation benchmark in the framework of the PRENOLIN Project [2], being the subsoil layering about horizontal (as checked by several MASW tests) and the S-wave propagation direction of the selected seismic records about vertical [2].

The upper part of the soil column is composed of loose gravel with a thickness of 1.25 m, overlying 5.9 m of a moderately dense fine sand (Fig. 14b). From 7.15 m in depth a stiff slate formation can be considered as the seismic bedrock. The ground water table is located at 1.45 m from the surface.

Downhole PS logging permitted to obtain the in-situ shear wave velocity profile; the stress-strain and strength properties were measured by laboratory tests on undisturbed samples [2].

The shear wave velocity profile adopted in the analysis (Fig. 14c) was obtained by adjusting the in-situ measurements, until showing a better agreement with the surface/borehole transfer function empirically obtained from weak-motion seismic records [2].

Undisturbed sand samples were retrieved at the depths of 3.3 and 5.4 m to carry out laboratory tests. Both samples were subjected to cyclic undrained triaxial tests to determine pre-failure stress-strain properties of soil; liquefaction and static strength were measured on the shallowest sample by means of stress-controlled cyclic undrained and consolidated-drained triaxial tests, respectively. A cohesion c' = 1.2 kPa and an internal friction angle φ' = 43.6° were obtained from the triaxial test.

The experimental data of laboratory tests are compared to the analytical curves predicted by the relevant constitutive models in Fig. 15.

The pre-failure cyclic triaxial tests were used to define the variation of normalized axial stiffness, E/E_0, and damping with strain level, ε_a.

Following the equivalence criteria between triaxial and simple shear tests [36], the axial strain was converted into shear strain as $\gamma = 1.5 \cdot \varepsilon_a$, while the ratio E/E_0 was assumed equal to G/G_0.

Figs. 15a,b show the good agreement between the MKZ model and the experimental data.

The cyclic resistance and pore pressure parameters were assigned to the fine sand layer on the basis of the results of the cyclic triaxial liquefaction tests (Figs. 15c,d).

The cyclic axial strength ratio was converted into an equivalent simple shear ratio through a correction factor equal to 0.64, i.e. the mean value of the factors computed adopting the procedures suggested by Castro [37] and Finn et al. [38].

As already observed for Nevada sand (Section 5), for the Sendai fine sand the experimental r_u : N/N_L relationship is not univocal, but strongly dependent on the cyclic stress ratio applied in each test (Fig. 15d). In this case, a unique mean curve was defined as the best-fit of the whole data set.

In lack of direct measurements, a permeability coefficient equal to $1 \cdot 10^{-5}$ m/s was adopted; the consolidation coefficient was computed through equation (30), by assigned E_{oed} through equation (31), with $\nu = 0.24$ and $K_0 = 0.31$ estimated from the friction angle through the Jaky [39] relationship.

In the one-dimensional analyses carried out by means of SCOSSA, the downhole acceleration records were applied as input motions. A rigid bedrock can be therefore assumed at the depth of 10.4 m, where the downhole sensor is located; the slate rock layer above the downhole sensor (7 ÷ 10.4 m) was instead modelled as a linear visco-elastic material, with constant damping equal to 1 %.

Six recorded input motions were selected, representing three different PGA levels (≥ 0.06, 0.02-0.03 g and ≤ 0.01 g) and two distinct frequency ranges [2].

The characteristics of the downhole and surface records are reported in Table 2, where the numbering of input motions corresponds to decreasing PGA amplitudes.

Figs. 16 and 17 compare the surface records versus the simulations of total stress analyses, for the low and high frequency content input motions, respectively.

The results are expressed in terms of acceleration time histories and spectral accelerations, both normalized with respect to the PGA recorded at surface.

For the low-frequency input signals, the surface motion predicted for input #1 (PGA= 0.251 g) strongly mobilizes the non-linear soil behaviour and overestimates by a factor of 1.5 the recorded PGA and the peak spectral acceleration attained between 0.1 and 0.2 s (Fig. 16a).

The predicted ground motions are in a good agreement with the records for the input signals #4 (Fig. 16b) and #8 (Fig. 16c), characterized by medium-low intensity.

The results of total stress analyses with the high-frequency input motions (Fig. 17) show an overall good prediction of the surface time histories and response spectra, except for the overestimation of spectral ordinates at periods lower than 0.15 s related to input #3.

The effective stress analyses were performed on the whole set of input motions, but excess pore pressure was triggered only for the records #1 and #3, i.e. those with the highest PGA (0.251 and 0.062 g). For all the other input motions, the results of effective stress analyses are practically coincident with those above shown.

The results of effective stress analyses for input motions #1 and #3 are compared in Fig. 18, with the recorded data and total stress simulations.

The comparisons demonstrate that the effective stress analyses predict the surface ground motion, with a definitely satisfying reproduction of the maximum recorded spectral accelerations and predominant periods.

7. Conclusion

A loosely-coupled approach to simulate liquefaction of saturated soils in one-dimensional seismic response analyses has been presented. The calculation steps required for numerical implementation and calibration of the model parameters are given in Sections 2 and 3. The main advantage is that the constitutive model is simple and requires a straightforward calibration of soil parameters with respect to those implemented in other numerical codes performing effective stress analyses. The soil properties required for the model calibration are the shear strength, the variation of the shear modulus and damping ratio with shear strain, consolidation coefficient, the cyclic resistance curve and the relationship between excess pore pressure and number of cycles.

The computer code SCOSSA was updated for predicting the seismic response of a horizontally layered subsoil across the whole range of possible shear strains, from the smallest amplitudes up to liquefaction.

The performance of the model and the code have been first tested on ideal soil profile under different drainage conditions, then validated by comparing the predictions with the results of a centrifuge test and the seismic motions recorded at a well-documented array station.

The overall good match between numerical and experimental results highlights the reliability of the model implemented in the code, notwithstanding the simplicity of the proposed approach.

As a future development, the loosely coupled formulation will be integrated in the 'slip' mode of the code [9], in order to predict also the permanent deformation mechanisms.

8. Acknowledgments

The Authors would like to thank Professors Steven L. Kramer and Pedro Arduino from University of Washington (Seattle, US) for their precious contribution in the development and verification of the 1D consolidation subroutine, which has been implemented in the computer code.

Professor Koji Ichii from Hiroshima University (Hiroshima, Japan) is gratefully acknowledged for his help in collecting the data about the site of Sendai.

The Authors wish finally to thank Professor Mahdi Taiebat from University of British Columbia (Vancouver, Canada) for providing data of the VELACS experiment.

9. References

[1] Régnier J, Bonilla L-F, Bard P-Y, Bertrand E, Hollender F, Kawase H, et al. International benchmark on numerical simulations for 1D, nonlinear site response (PRENOLIN): verification phase based on canonical cases. Bull Seismol Soc Am 2016;106(5):2112–2135. DOI: https://doi.org/10.1785/0120150284.

[2] Régnier J, Bonilla L-F, Bard P-Y, Bertrand E, Hollender F, Kawase H, et al. PRENOLIN: International benchmark on 1D nonlinear site-response analysis - Validation phase exercise. Bull Seismol Soc Am 2018;108(2):876-900. DOI: https://doi.org/10.1785/0120170210.

[3] Hashash YMA, Musgrove MI, Harmon JA, Groholski DR, Phillips CA, Park D DEEPSOIL 6.1, User Manual. Urbana, IL, Board of Trustees of University of Illinois at Urbana-Champaign; 2016.

[4] ITASCA Consulting Group Inc. FLAC 8.0 - Fast Lagrangian Analysis of Continua. Minneapolis, MN, USA; 2016.

[5] Brinkgreve RBJ, Engin E, Swolfs WM. PLAXIS 2D Reference Manual; 2016.

[6] GEOSLOPE International Ltd. Dynamic modeling with QUAKE/W. Calgary, Alberta, Canada; 2012.

[7] Kavazanjian E, Andrade JE, Arulmoli K, Atwater BF, Christian JT, Green R, et al. State of the art and practice in the assessment of earthquake-induced soil liquefaction and its consequences. National Academy of Sciences; 2016. DOI: 10.17226/23474.

[8] Terzaghi K, Theoretical Soil Mechanics. John Wiley & Sons; 1943.

[9] Tropeano G, Chiaradonna A, d'Onofrio A, Silvestri F. An innovative computer code for 1D seismic response analysis including shear strength of soils. Geotechnique 2016;66(2):95–105. http://dx.doi.org/10.1680/jgeot.SIP.15.P.017.

[10] Kuhlemeyer RL, Lysmer J. Finite Element Method Accuracy for Wave Propagation Problems. J Soil Mech Found Div 1973;99(SM5):421–427.

[11] Hashash YMA, Park D. Viscous damping formulation and high frequency motion propagation in non-linear site response analysis. Soil Dyn Earthq Eng 2002;22(7):611–624.

[12] Newmark NM. A Method of Computation for Structural Dynamics. J Eng Mech Div 1959; 85(EM7):67–94.

[13] Kondner RL, Zelasko JS. Hyperbolic stress-strain formulation of sands. In Proceedings of the 2nd Panamerican Conference on Soil Mechanics and Foundation Engineering, Sao Paulo, Brazil. Associação Brasileira de Mecânica dos Solos 1963;1:289-324.

[14] Pyke RM. Nonlinear soil model for irregular cyclic loadings. J Geotech Eng Div 1979;105(6): 715–726.

[15] Matasovic N, Vucetic M. Cyclic Characterization of Liquefiable sands. J Geotech Eng 1993;119(11):1805–1822.

[16] Lee MKW, Finn WDL. DESRA-2 Dynamic Effective Stress Response Analysis of soil deposits with energy transmitting boundary including assessment of liquefaction potential. Soil Mech Series. Department of Civil Engineering, University of British Columbia, Canada; 1978.

[17] Matasovic N, Ordonez GA. DMOD 2000: A Computer Program for Nonlinear Seismic Response Analysis of Horizontally Layered Soil Deposits, Earthfill Dams and Solid Waste Landfills. Lacey, WA: GeoMotions, LLC; 2011.

[18] Phillips C, Hashash YMA. Damping formulation for nonlinear 1D site response analyses. Soil Dyn Earthq Eng 2009;29(7):1143–1158.

[19] Moreno-Torres O, Hashash YMA, Olson SM. A simplified coupled soil-pore water pressure generation for use in site response analysis. In Proceedings GeoFlorida 2010: Advanced in Analysis, Modeling & Design 2010, p. 3080–3089.

[20] Gingery JR, Elgamal A. Shear Stress-Strain Curves Based on the G/Gmax Logic: A Procedure for Strength Compatibility. In Proceedings of the 2th International Conference on Geotechnical and Earthquake Engineering, IACGE, Chengdu, China, 2013, p. 1–9.

[21] Stewart JP, Kwok AO, Hashash YMA, Matasovic N, Pyke R, Wang Z, et al. Benchmarking of Nonlinear Geotechnical Ground Response Analysis Procedures. PEER Report 2008/04 Pacific Earthquake Engineering Research Center College of Engineering, University of California, Berkeley 2008.

[22] Hashash YMA, Phillips C, Groholski DR. Recent advances in non-linear site response analysis. In Proceedings of the Fifth Int Conf Recent Adv Geotech Earthq Eng Soil Dyn 2010;29(6):1–22.

[23] Groholski DR, Hashash YMA, Kim B, Musgrove M, Harmon J, Stewart JP. Simplified Model for Small-Strain Nonlinearity and Strength in 1D Seismic Site Response Analysis. J Geotech Geoenvironmental Eng 2016;142(9). DOI: 10.1061/(ASCE)GT.1943-5606.0001496.

[24] Hardin BO, Drnevich V. Shear modulus and damping in soils: design equations and curves. J Soil Mech Found Div 1972;98(SM7):667–691.

[25] Tonni L, Gottardi G, Amoroso S, Bardotti R, Bonzi L, Chiaradonna A, et al. Analisi dei fenomeni deformativi indotti dalla sequenza sismica emiliana del 2012 su un tratto di argine del Canale Diversivo di Burana. Italian Geotech J 2015;49(2)28–58 (in Italian).

[26] Chiaradonna A, Tropeano G., d'Onofrio A, Silvestri F. Development of a simplified model for pore water pressure build-up induced by cyclic loading. Bull Earthq Eng https://doi.org/10.1007/s10518-018-0354-4.

[27] Porcino D, Diano V. Laboratory Study on Pore Pressure Generation and Liquefaction of Low-Plasticity Silty Sandy Soils during the 2012 Earthquake in Italy. J Geotech Geoenvironmental Eng 2002;142(10). https://doi.org/10.1061/(ASCE)GT.1943-5606.0001518.

[28] Das BM. Advanced Soil Mechanics. 3rd ed. Taylor & Francis Group; 2008.

[29] Chiaradonna A. Development and assessment of a numerical model for non-linear coupled analysis on seismic response of liquefiable soils. Ph.D. Thesis, Naples, Italy: University of Napoli Federico II; 2016.

[30] Elgamal A, Zeghal M, Taboada V, Dobry R. Analysis of Site Liquefaction and Lateral Spreading Using Centrifuge Testing Records. Soils Found 1996;36(2):111–121.

[31] Arulmoli K, Muraleetharan KK, VELACS Laboratory testing program Soil data report. Earth Technology Corporation; 1992.

[32] Taboada VM. Centrifuge modeling of earthquake-induced lateral spreading in sand using a laminar box. Ph.D. Thesis, Rensselaer Polytechnic Institute, Troy, NY;1995.

[33] Taiebat M, Shahir H, Pak A. Study of pore pressure variation during liquefaction using two constitutive models for sand. Soil Dyn Earthq Eng 2007;27(1):60–72.

[34] Boulanger RW, Idriss IM. CPT-Based Liquefaction Triggering Procedure. J Geotech Geoenvironmental Eng 2016;142(2):4015065.

[35] OYO Corporation. Report of soil investigation: Sendai District and Onahama District. Report from the PRENOLIN Project, Nice, France; 2014.

[36] Silvestri F. Looking for objective criteria in the interpretation of laboratory stress-strain tests. Pre-failure deformation characteristics of geometerials. Jamiolkowski, Lancellotta e Lo Presti (eds). Swets and Zeitlinger, Lisse; 2001 ISBN 9058090752.

[37] Castro G. Liquefaction and cyclic mobility of sands. J Geotech Eng Div 1975;101(GT6):552-569.

[38] Finn WDL, Pickering DJ, Bransby PL. Sand liquefaction in triaxial and simple shear tests. J Soil Mech Found Div 1971;97(SM4):639-659.

[39] Jaky J. Pressure in silos, In: Proceedings of the second International Conference on Soil Mechanics and Foundation Engineering, 1948.

Figure captions

Fig. 1. Layered soil column (a) modelled as a multi-degree of freedom system for dynamic equilibrium (b) and as a multilayered continuous system (c) for consolidation

Fig. 2. Flowchart of the numerical algorithm

Fig. 3. (a) Shear stress-strain cycles and (b) time histories of shear strain and excess pore water pressure ratio in total (decoupled approach) and effective stress analysis (coupled undrained approach).

Fig. 4. Normalized shear modulus reduction (a) and shear stress vs. shear strain (b) curves computed using the best-fitting calibration procedure of the MKZ model and adjustment according to Gingery and Elgamal [18]

Fig. 5. Cyclic stress ratio vs. number of cycles (a) and excess pore pressure ratio relationship (b) for a silty sand (data from [27] *)*

Fig. 6. Model performance under a regular saw-tooth shear stress history (a): time histories of shear stress ratio and damage parameter (b); normalized damage parameter (c); excess pore pressure (d)

Fig. 7. Profiles of V_S (a) and shear strength (b); input motion (c); variation of normalized stiffness and damping with shear strain (d)

Fig. 8. Profiles resulting from total decoupled and effective coupled stress analyses: maximum (a) acceleration, (b) shear strain, (c) shear stress, (d) pore pressure ratio; Time histories of shear stress and pore pressure at 3 m depth for (a) total stress analysis, (b) effective stress analysis in undrained conditions and (c) effective stress analysis with dissipation of excess pore pressure

Fig. 9. Cross section of the centrifuge laminar box

Fig. 10. Soil model and V_S profile (a), reference input motion (b), G_0 - p' relationship (c)

Fig. 11. Laboratory results vs. constitutive model for Nevada sand: resonant column test data (a); normalized shear modulus and damping (b); cyclic resistance curve (c); pore pressure relationship (d)

Fig. 12. Recorded and computed excess pore pressure time histories during the first 20 s (a) and until attainment of dissipation (b)

Fig. 13. Recorded and simulated acceleration time histories at the surface (a), 2.3 m (b) and 4.6 m (c)

Fig. 14. Location of Sendai in Japan with location of the Sendai vertical array (a); soil model (b) and V_S profile (c)

Fig. 15. Sendai array sand: results and interpretation of pre-failure (a) and liquefaction (b,c) cyclic triaxial tests

Fig. 16. Sendai array site, low frequency input motions: time histories and response spectra recorded at surface vs. those simulated by total stress analyses

Fig. 17. Sendai array site, high frequency input motions: time histories and response spectra recorded at surface vs. those simulated by total stress analyses

Fig. 18. Sendai array site, strongest input motions: time histories and response spectra recorded at surface vs. those simulated by total and effective stress analyses

Tables

Table 1. Main soil parameters

Parameter	Silty sand	Bedrock
Dry unit weight, γ_d (kN/m^3)	17.73	22.00
Porosity, n	0.32	-
Shear wave velocity, V_S (m/s)	See Fig. 7a	800
Friction angle, φ (°)	34.6	-
Coefficient of earth pressure at the rest, K_0	0.43	-
Poisson's ratio, ν	0.3	-
Permeability, k (m/s)	1×10^{-5}	∞
Small strain damping ratio, D_0 (%)	1.9	0.5
Cyclic strength parameters	$\alpha = 1.99$; $CSR_t = 0.10$	-
Pore pressure parameters	a = 1.07; b = 0.53; c = -0.12; d = 4	-

Table 2. EW components of the downhole and surface records

Record	Frequency content	downhole PGA [g]	surface PGA [g]
1	Low	0.251	0.405
4		0.025	0.075
8		0.005	0.009
3	High	0.062	0.183
6		0.035	0.074
7		0.012	0.033

Figure_1

Click here to download high resolution image

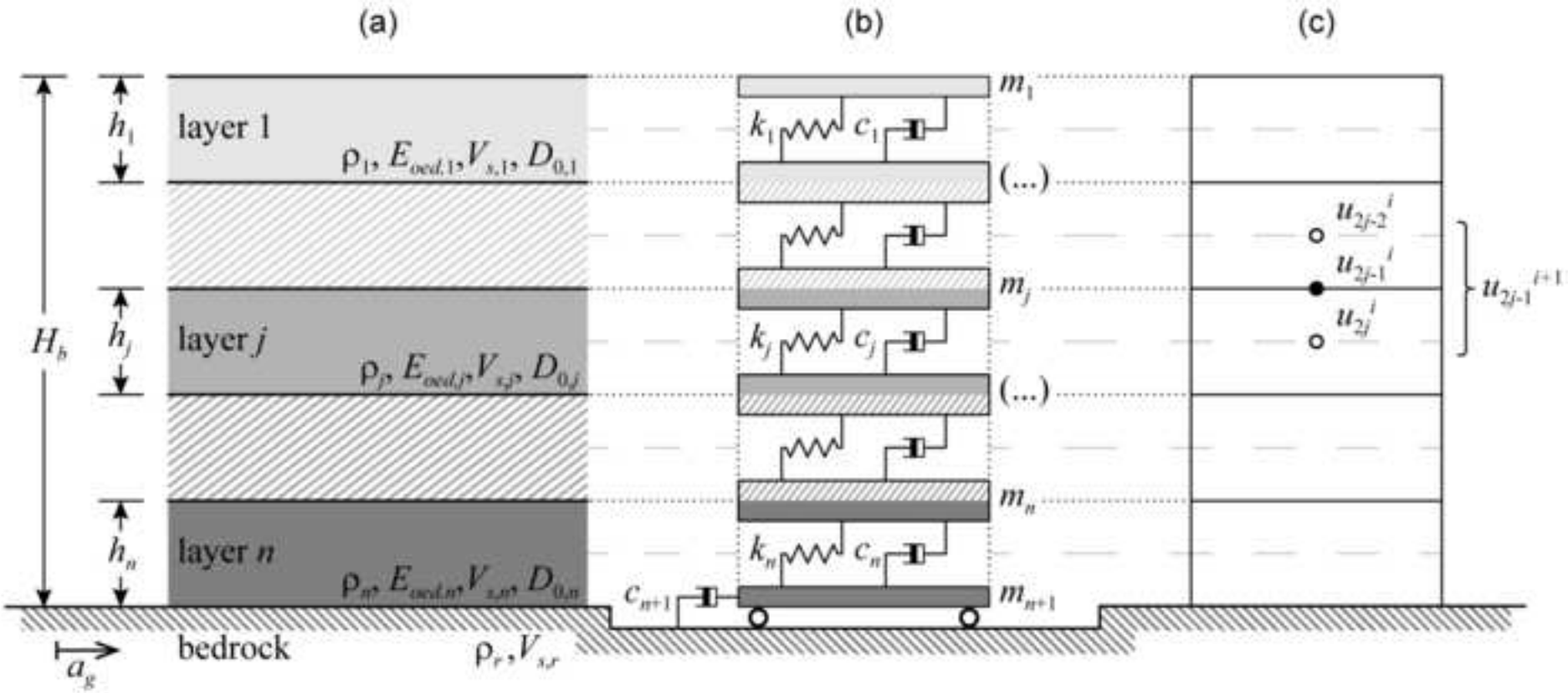

Figure_2
Click here to download high resolution image

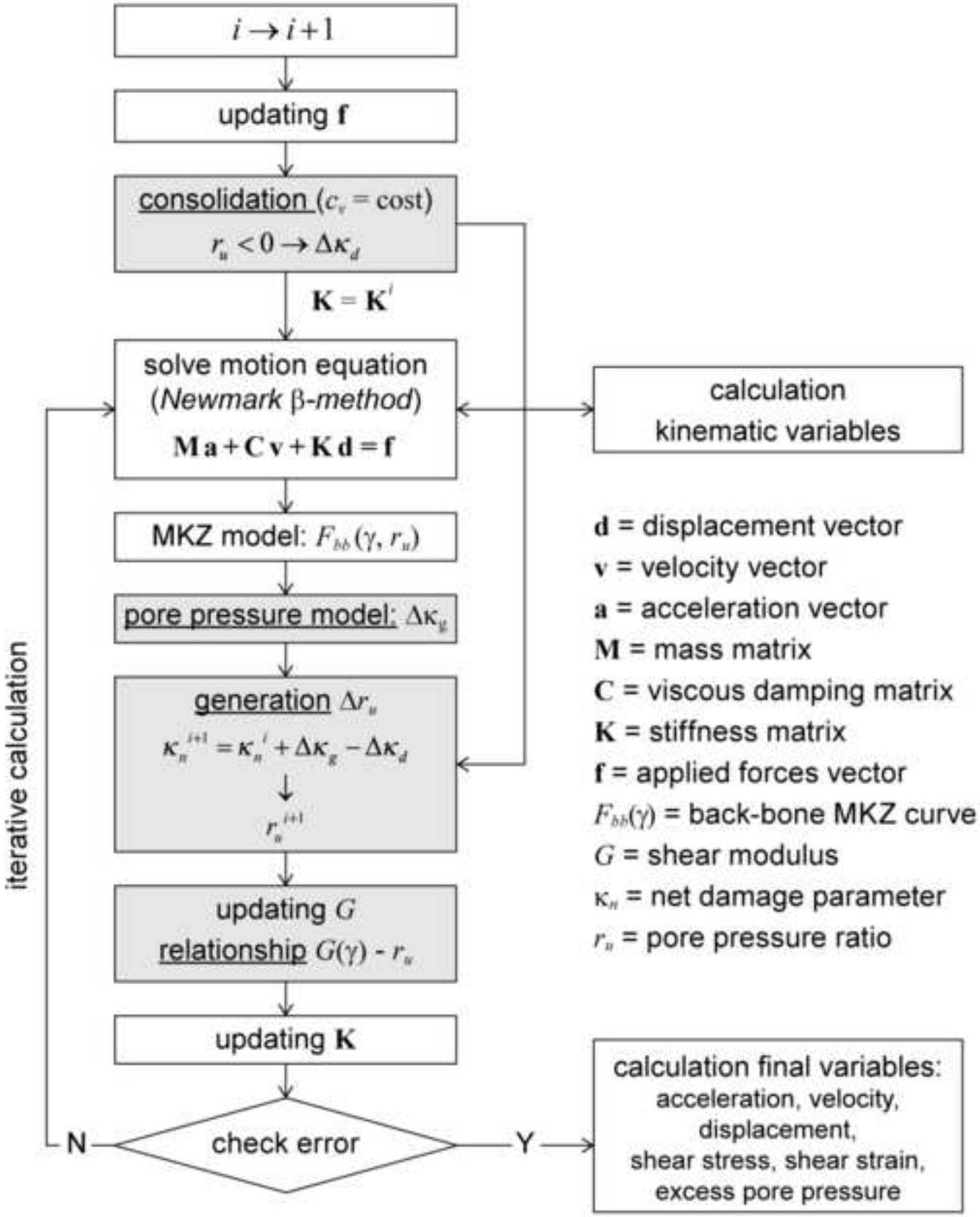

Figure_3
Click here to download high resolution image

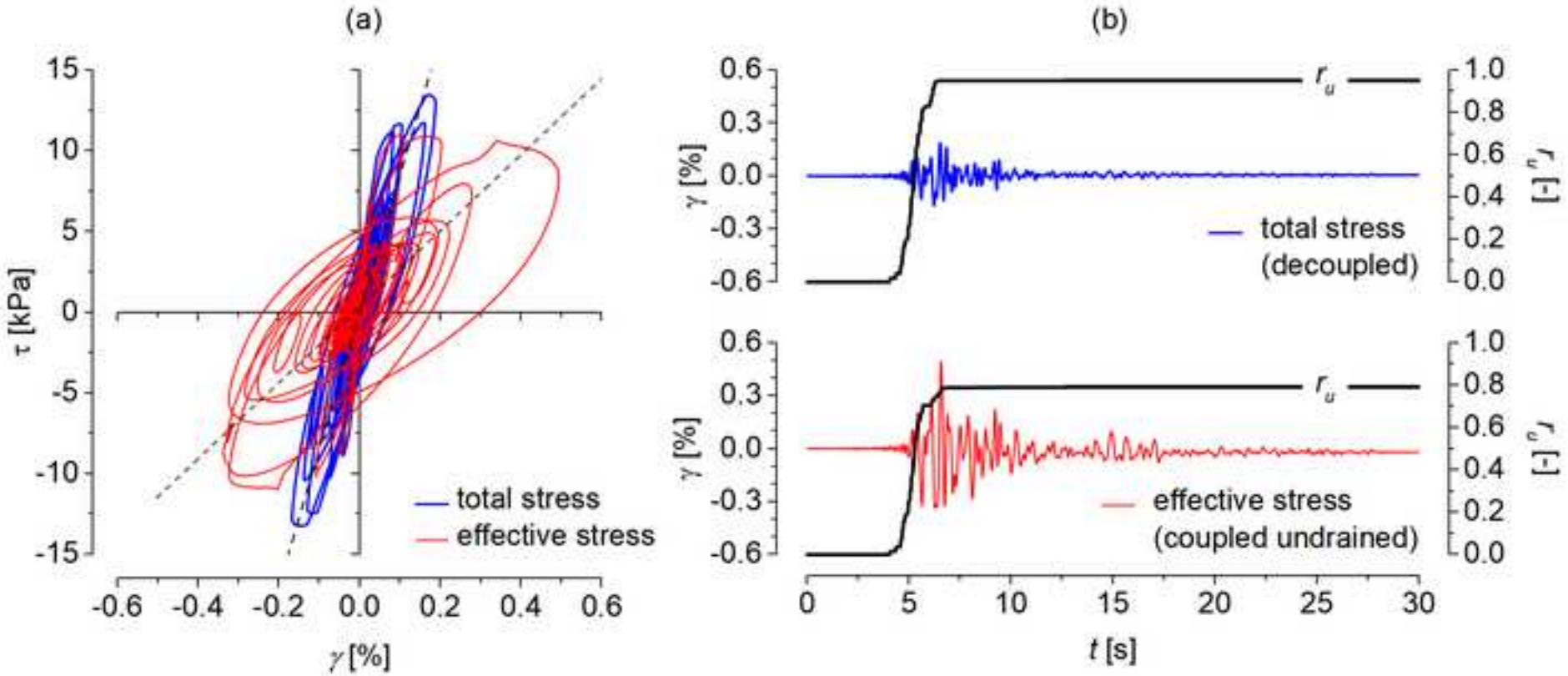

Figure_4
Click here to download high resolution image

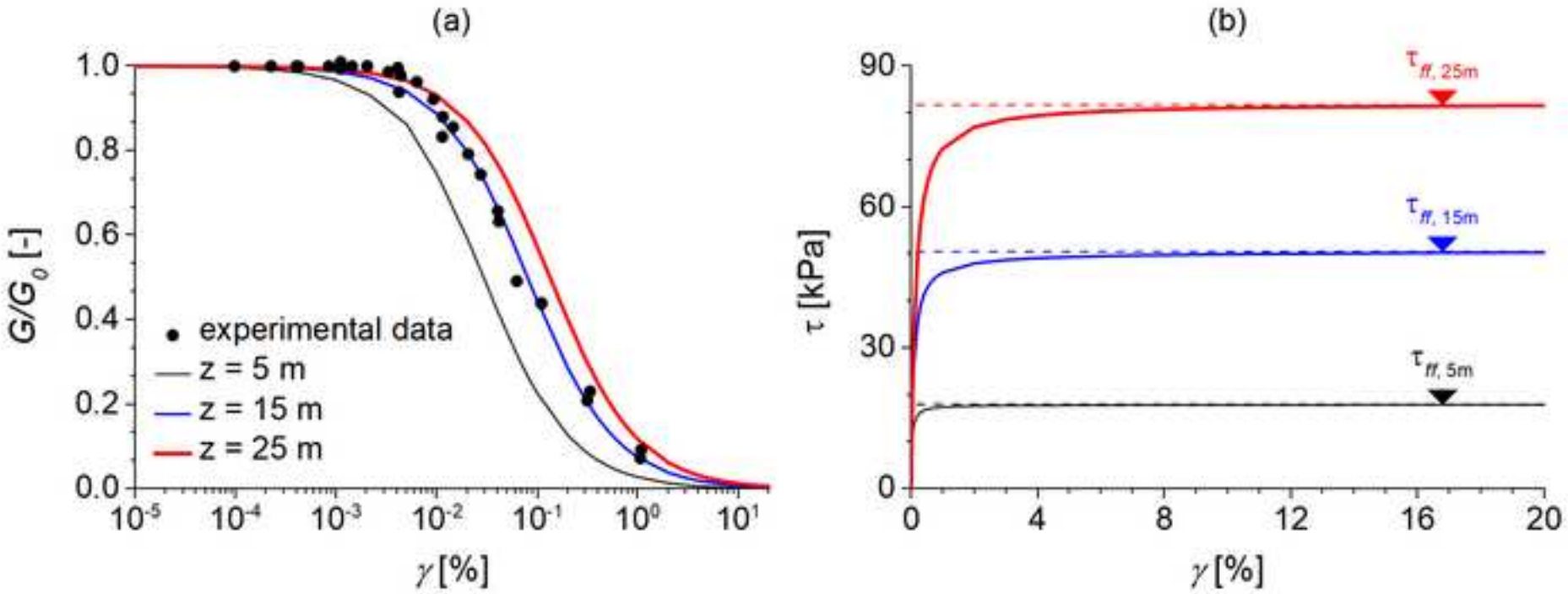

Figure_5
Click here to download high resolution image

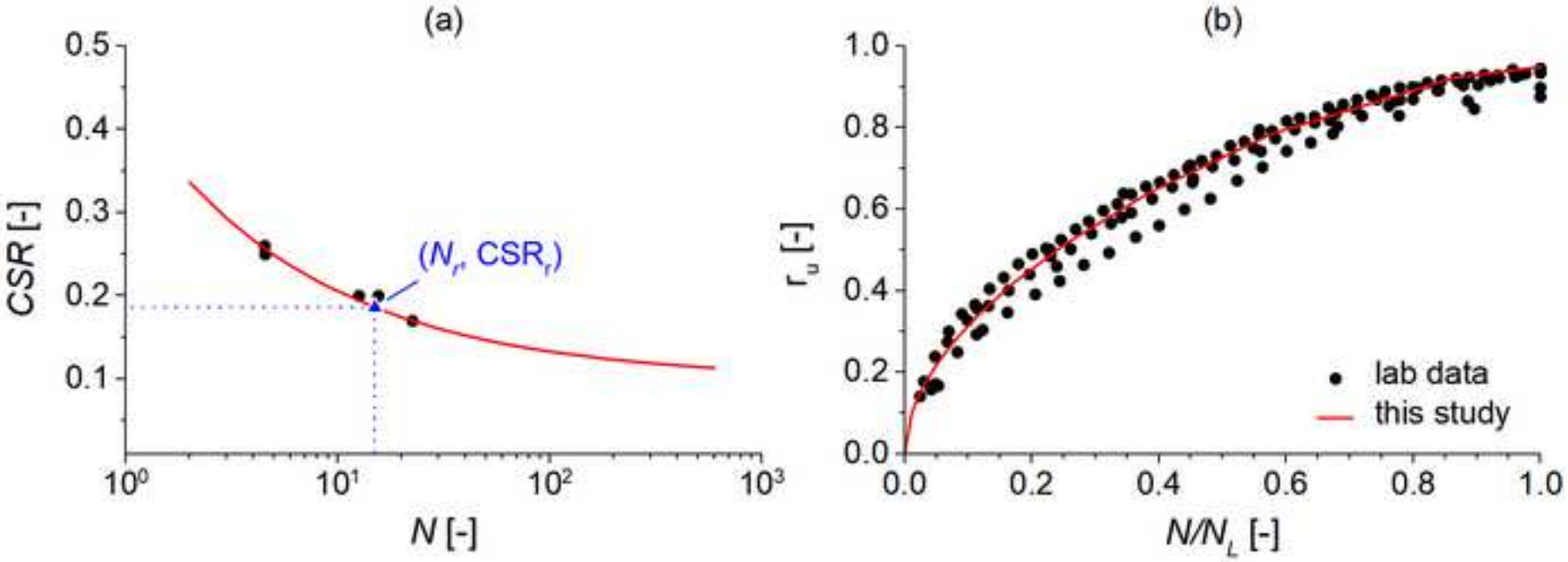

Figure_6
Click here to download high resolution image

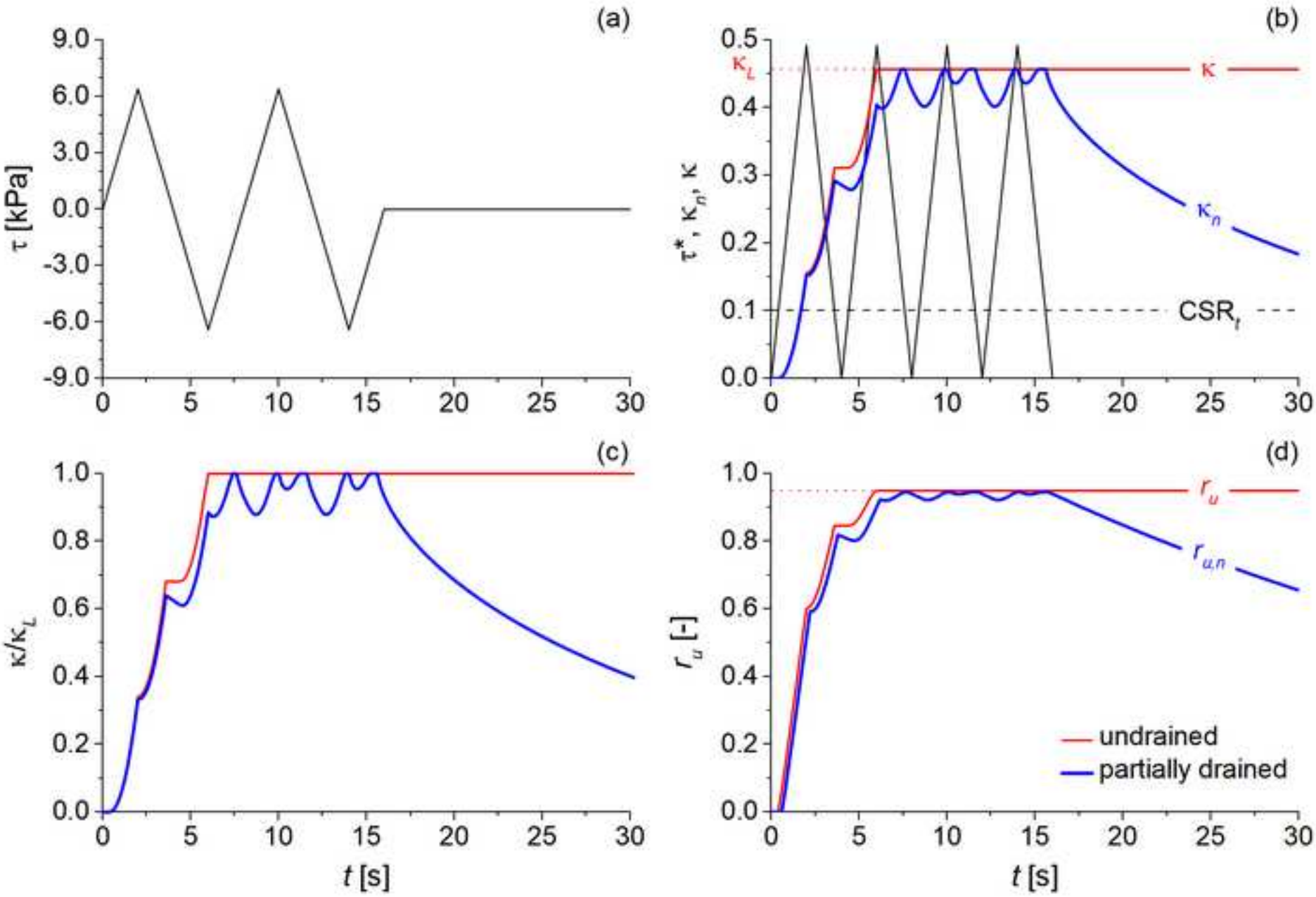

Figure_7

Click here to download high resolution image

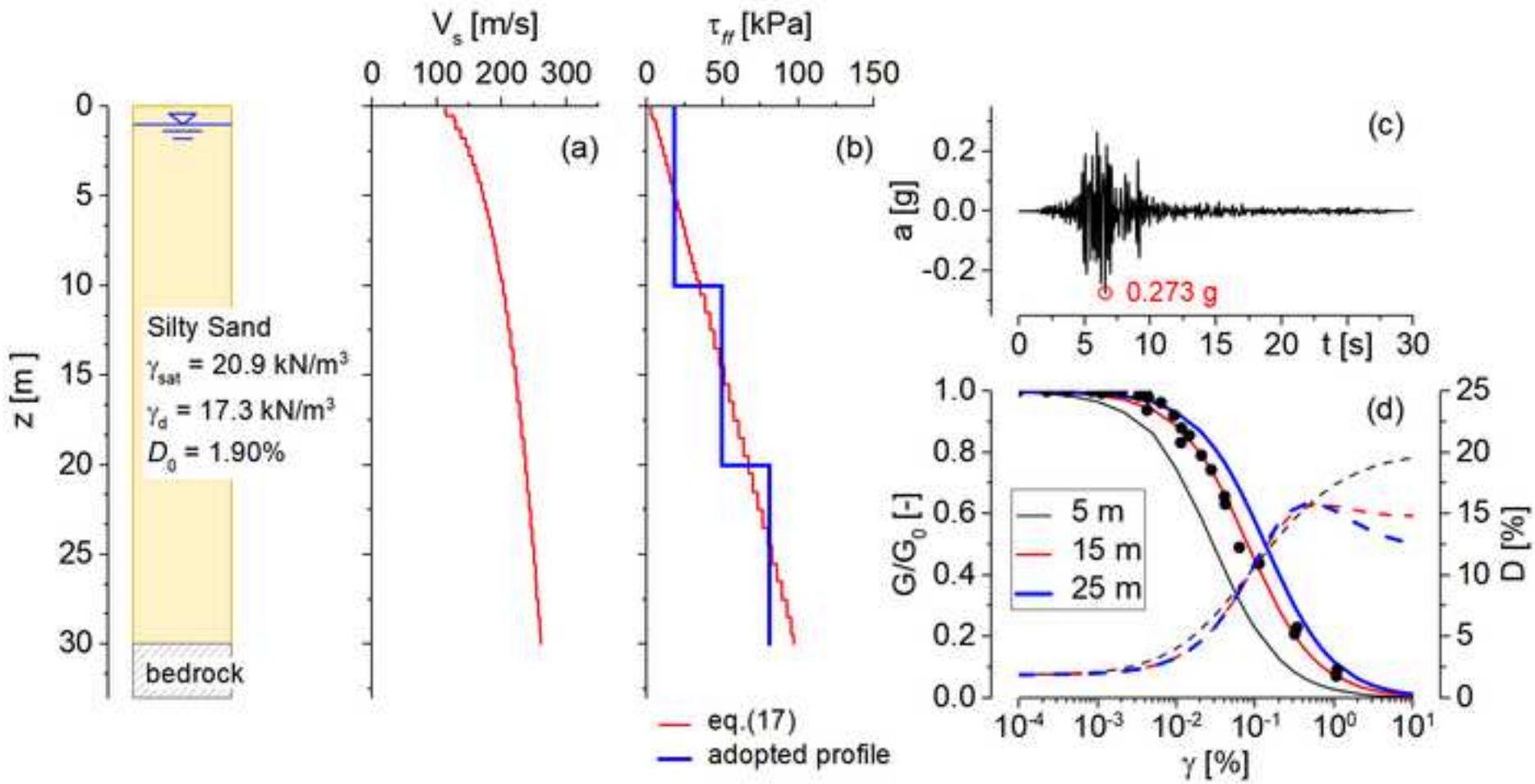

Figure_8

Click here to download high resolution image

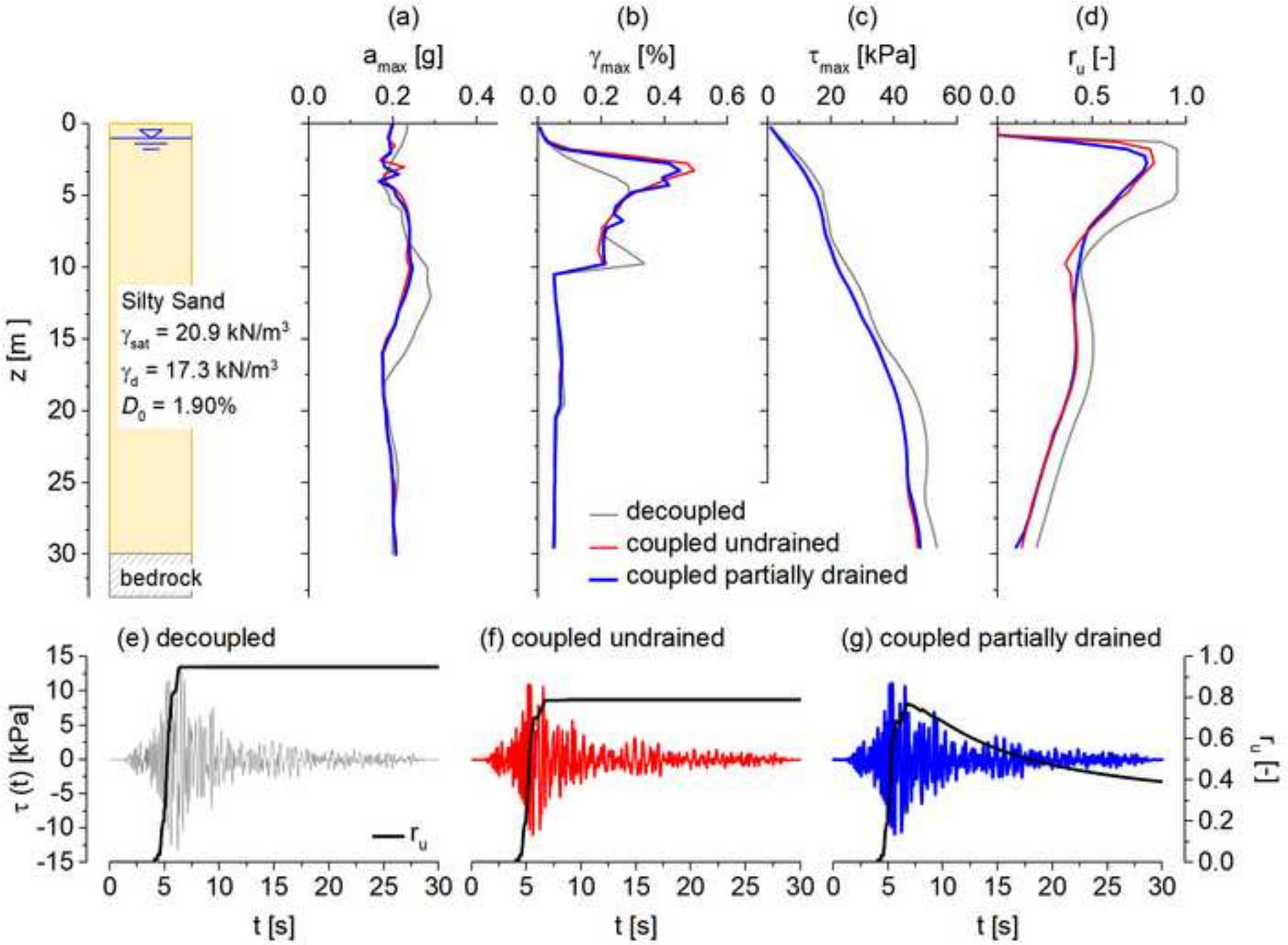

Figure_9
Click here to download high resolution image

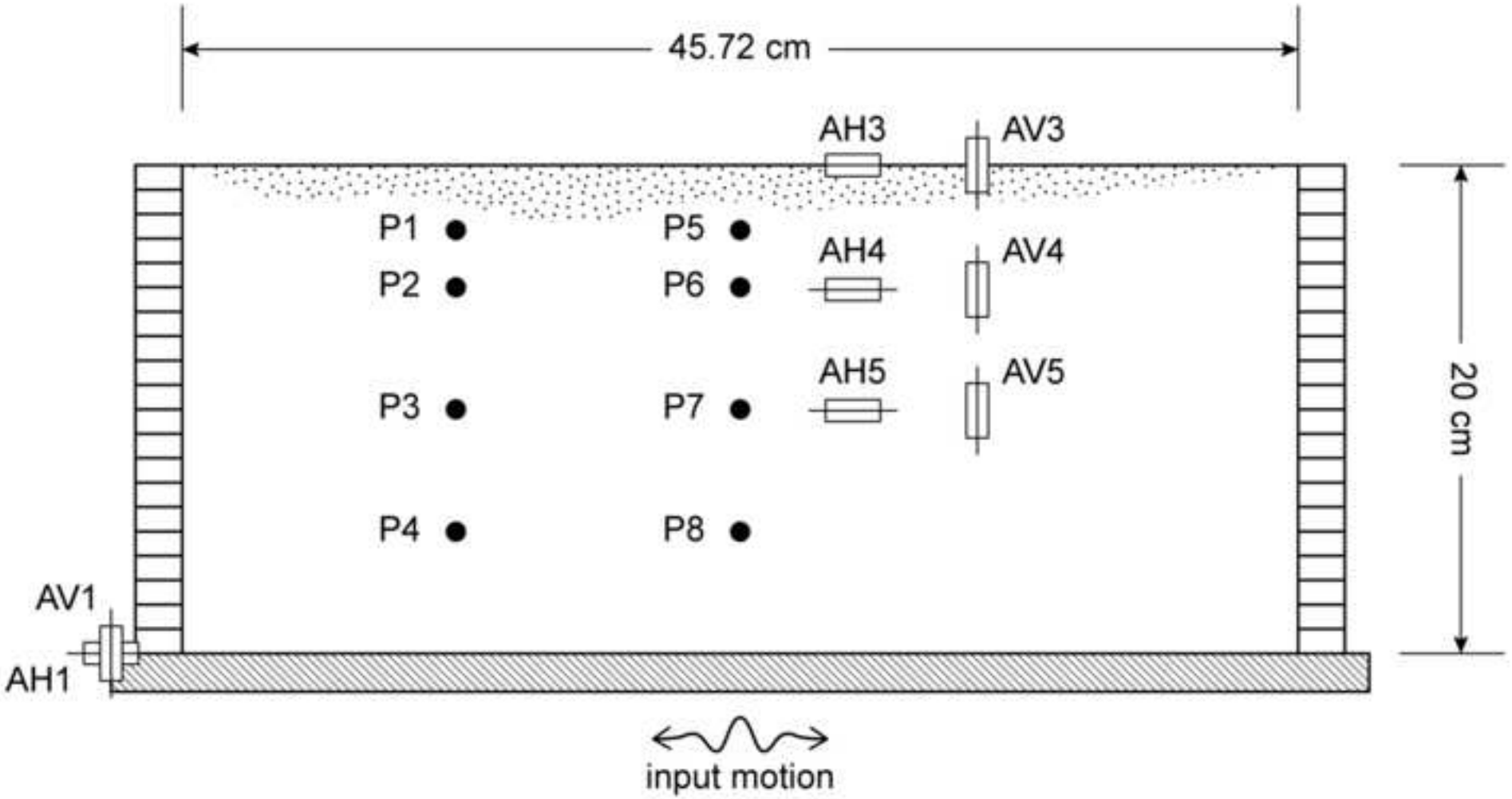

Figure_10
Click here to download high resolution image

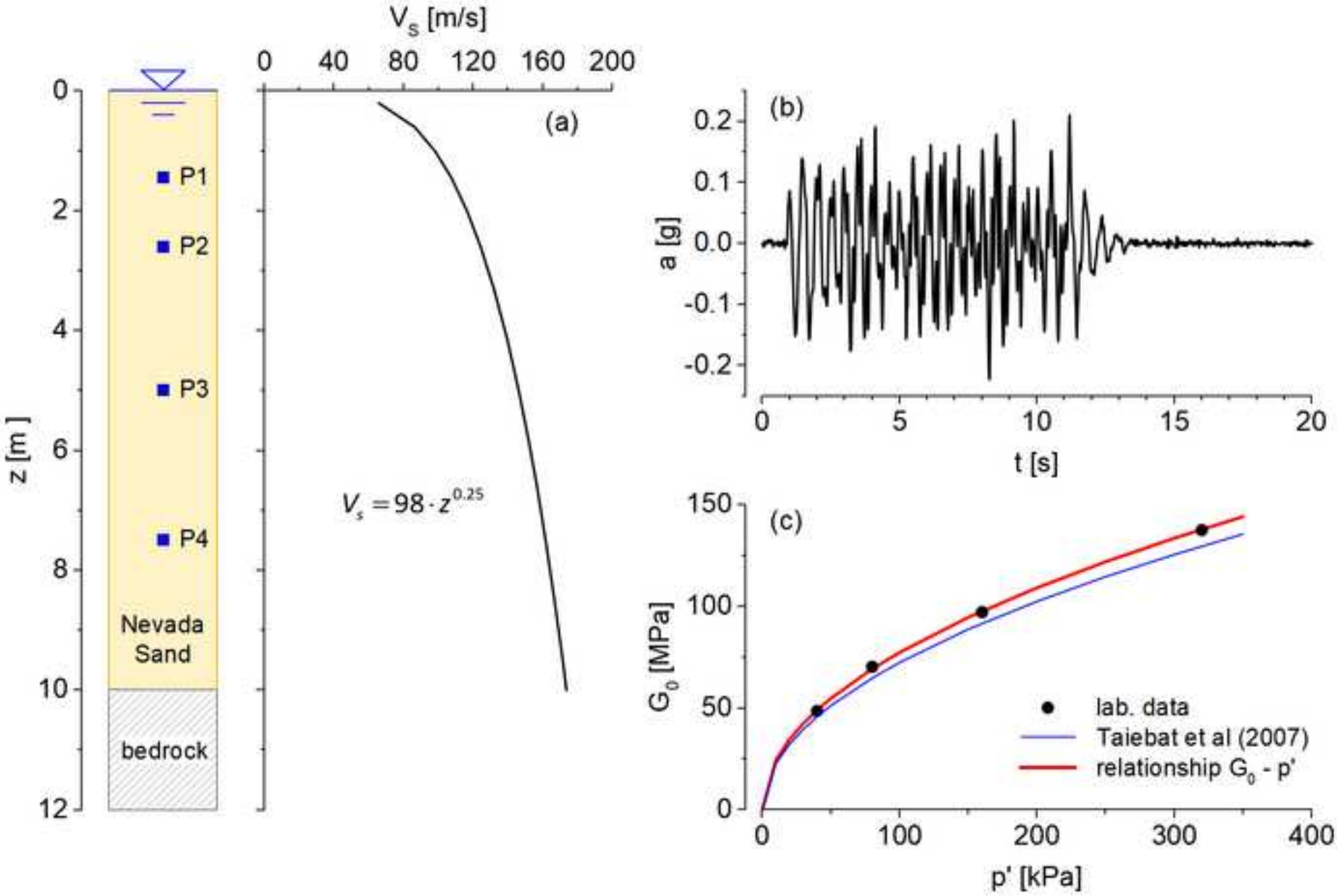

Figure_11
Click here to download high resolution image

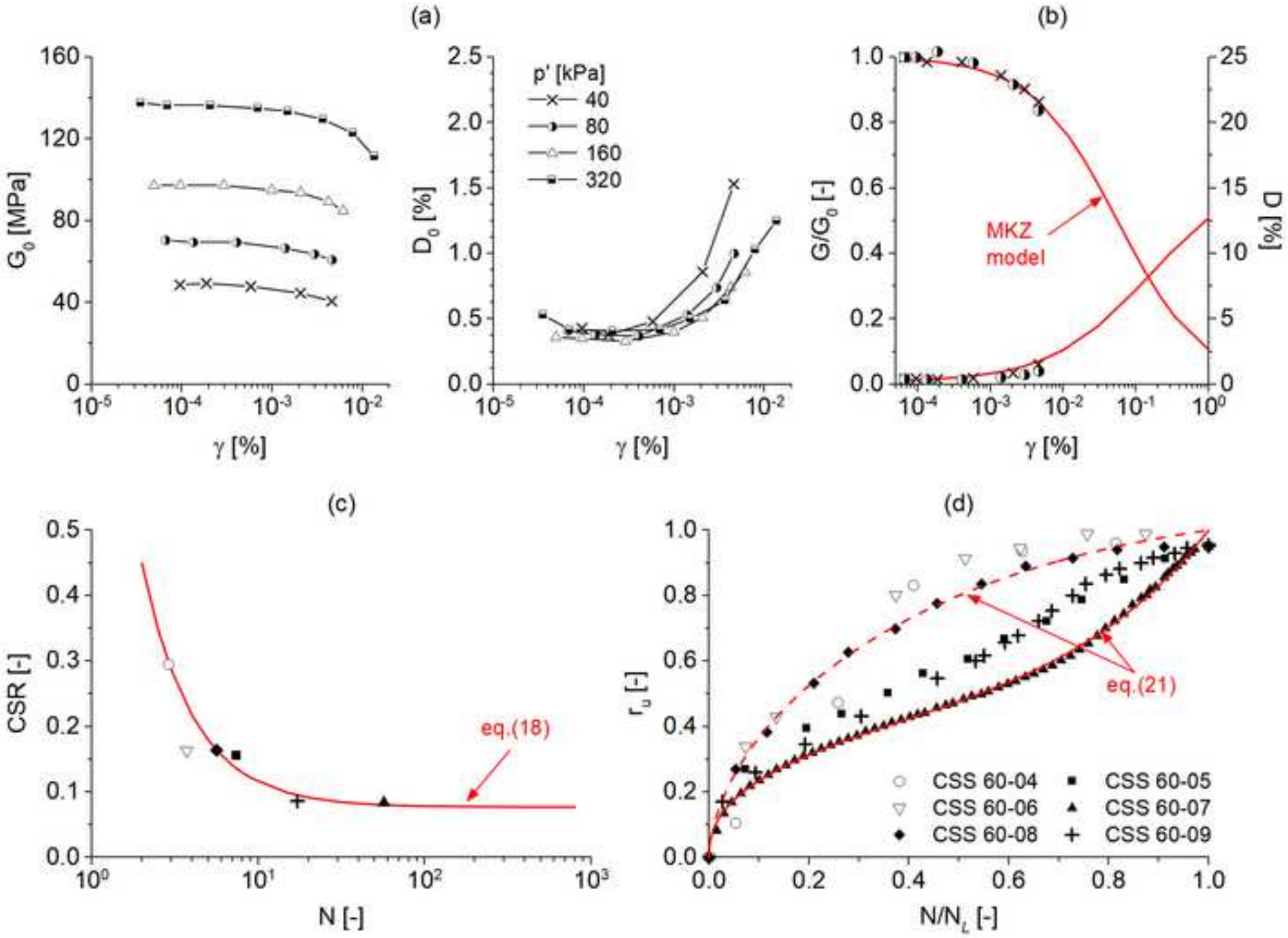

Figure_12
Click here to download high resolution image

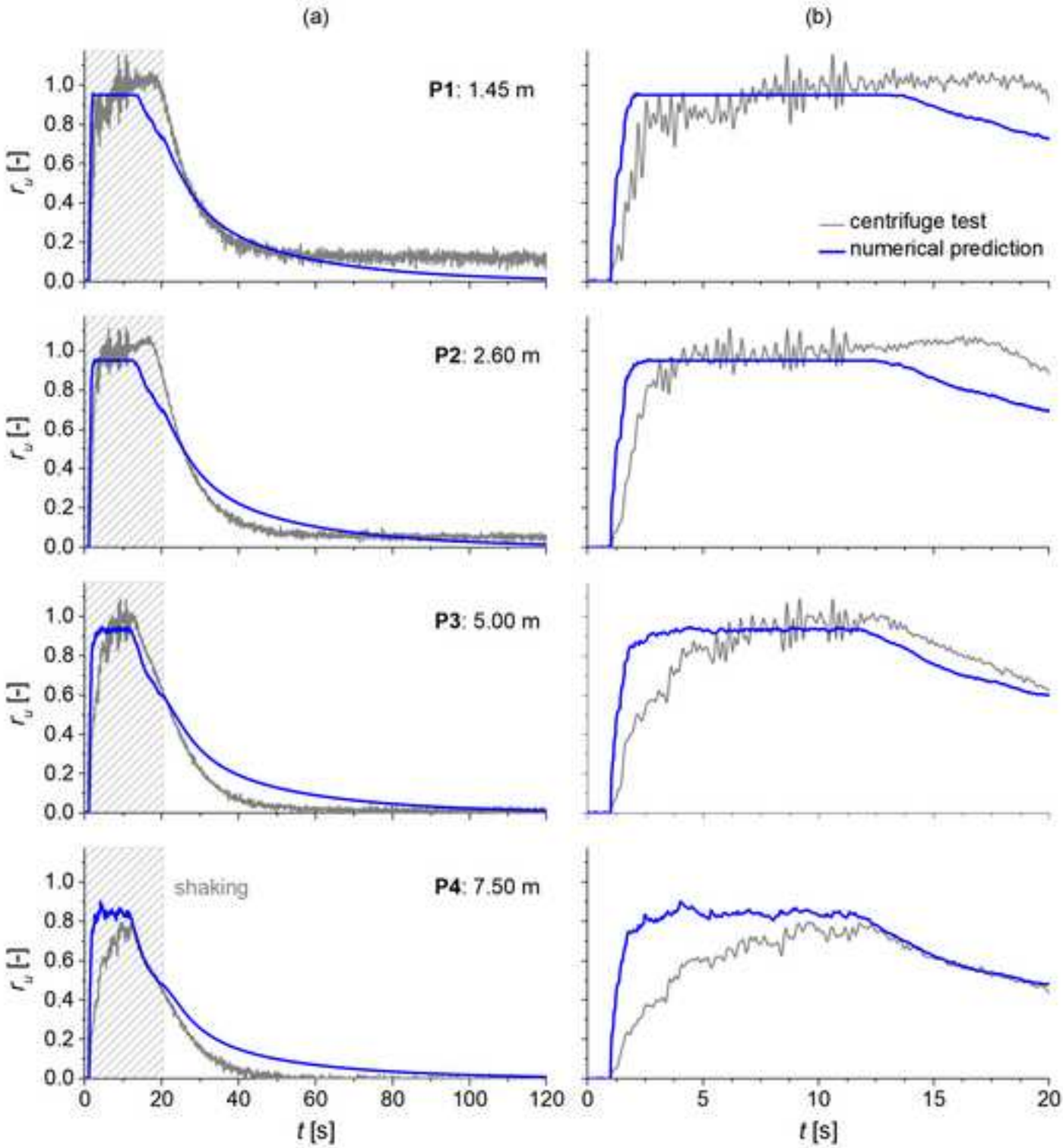

Figure_13
Click here to download high resolution image

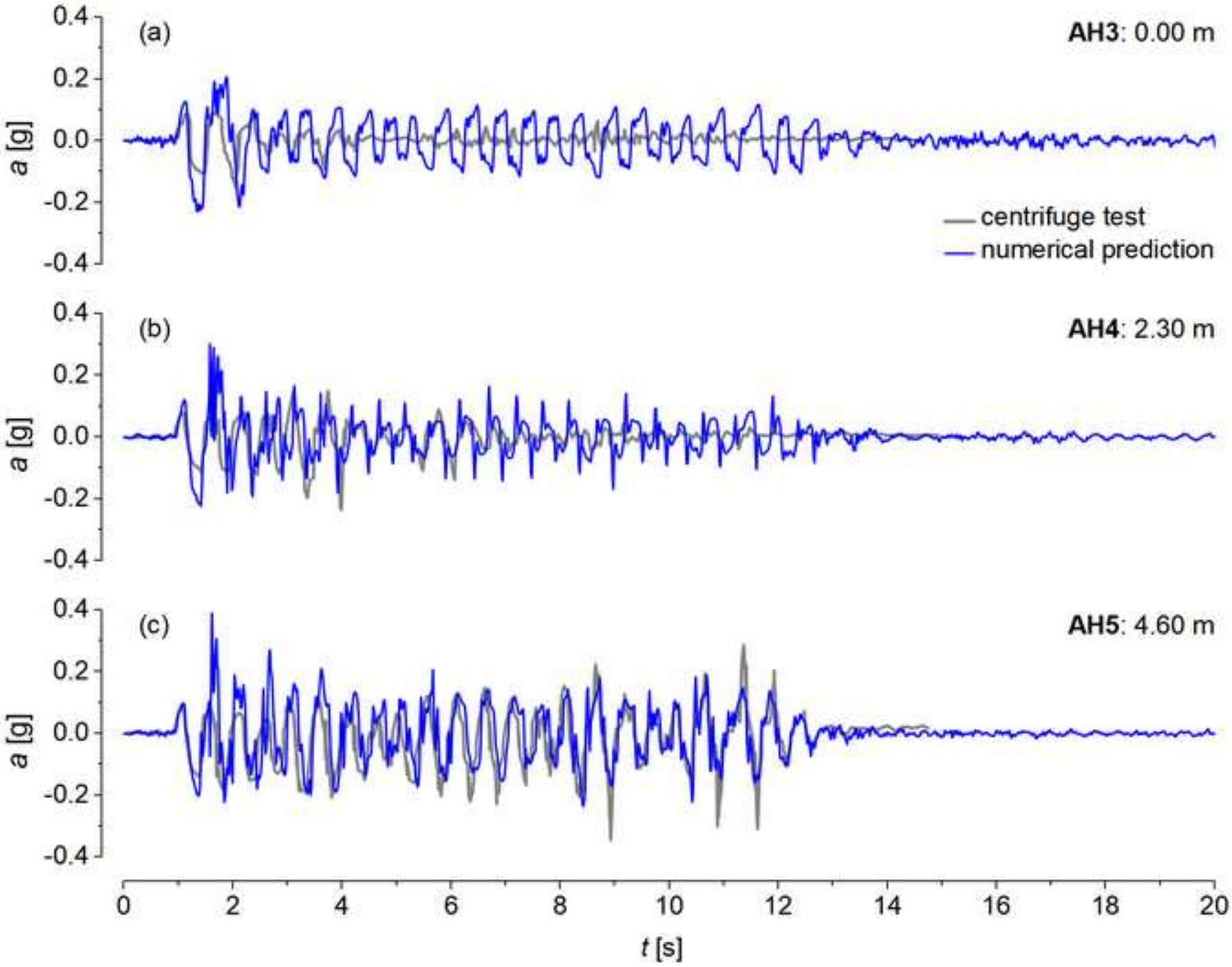

Figure_14
Click here to download high resolution image

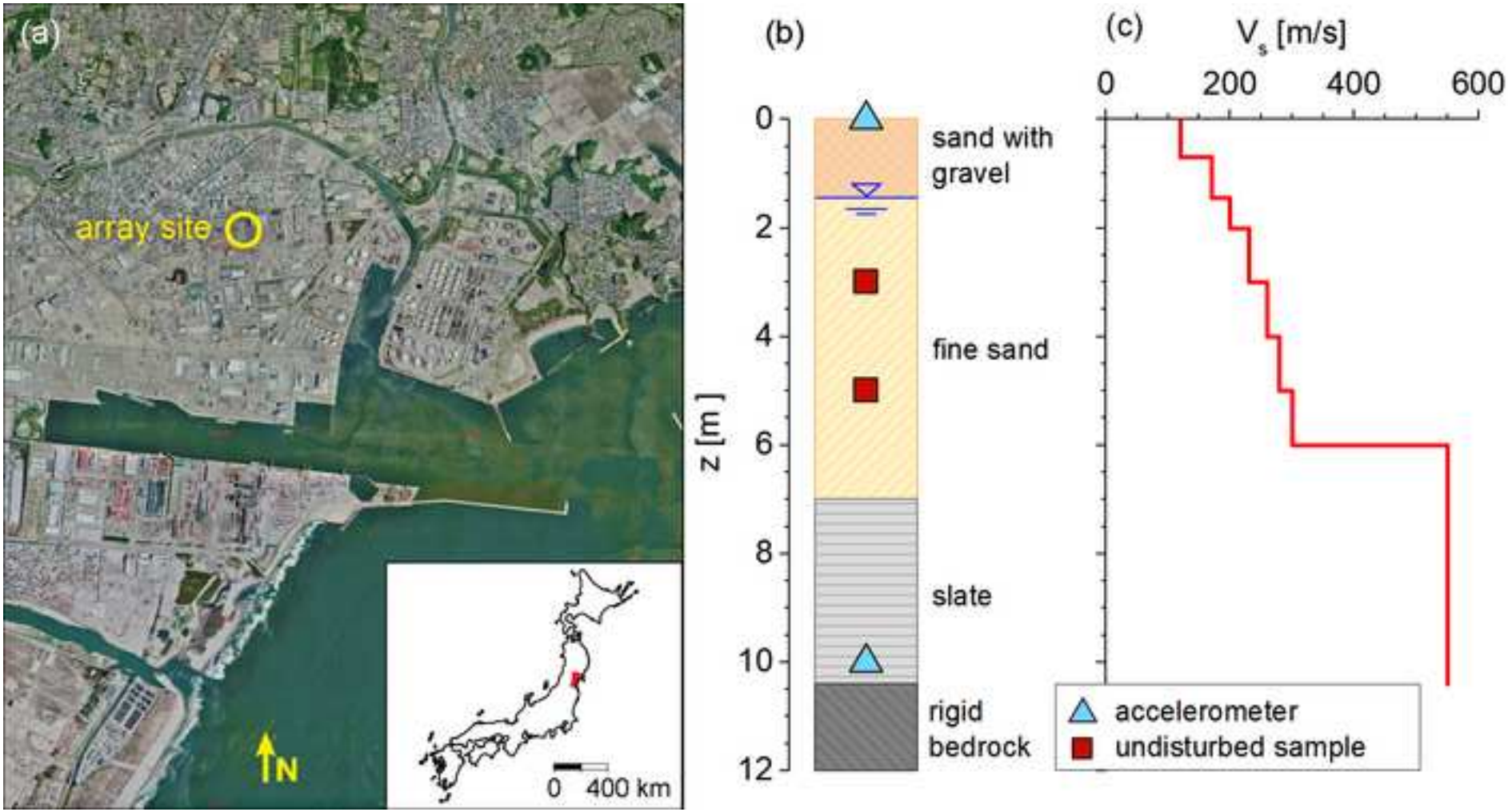

Figure_15
Click here to download high resolution image

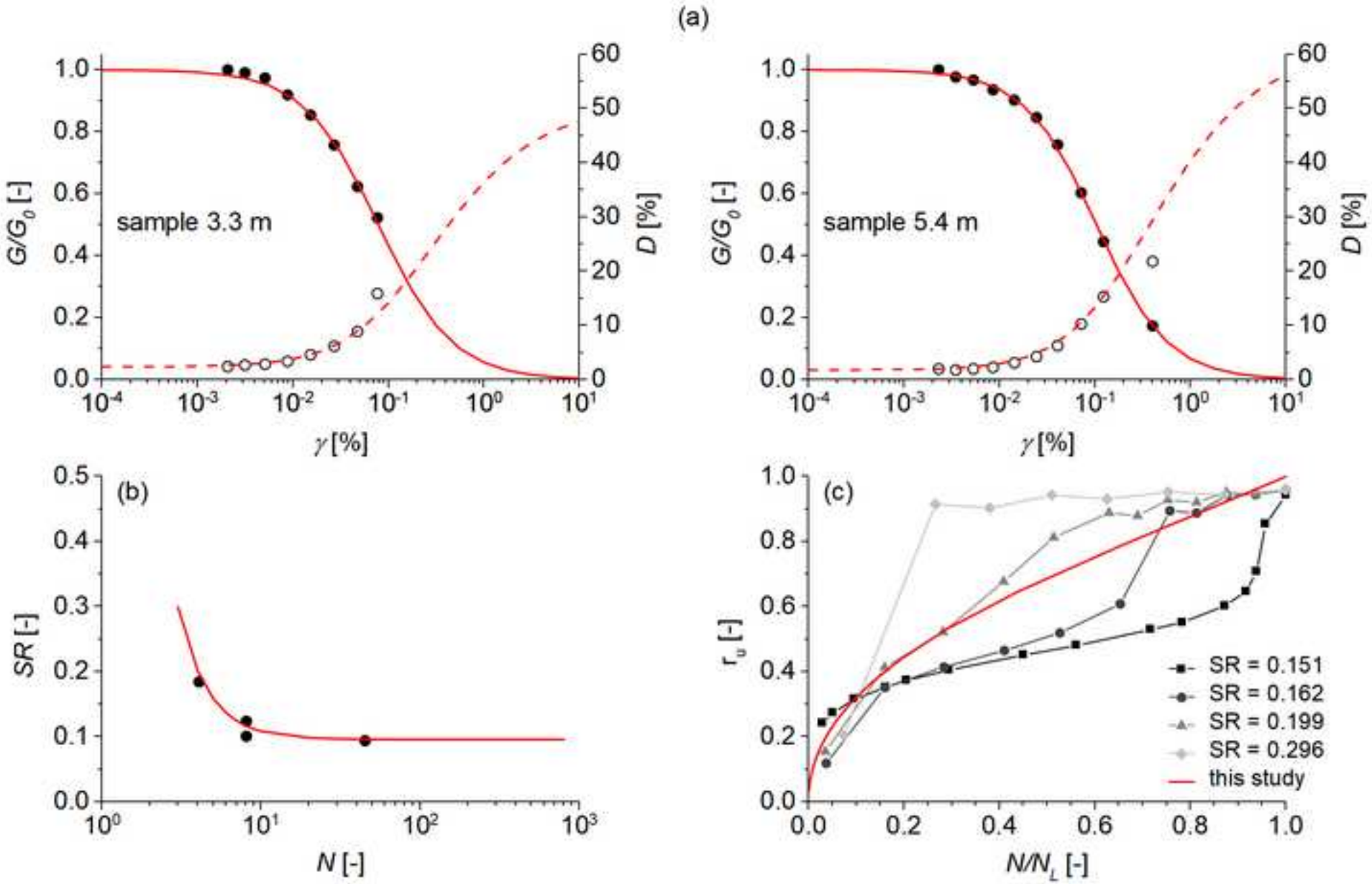

Figure_16
Click here to download high resolution image

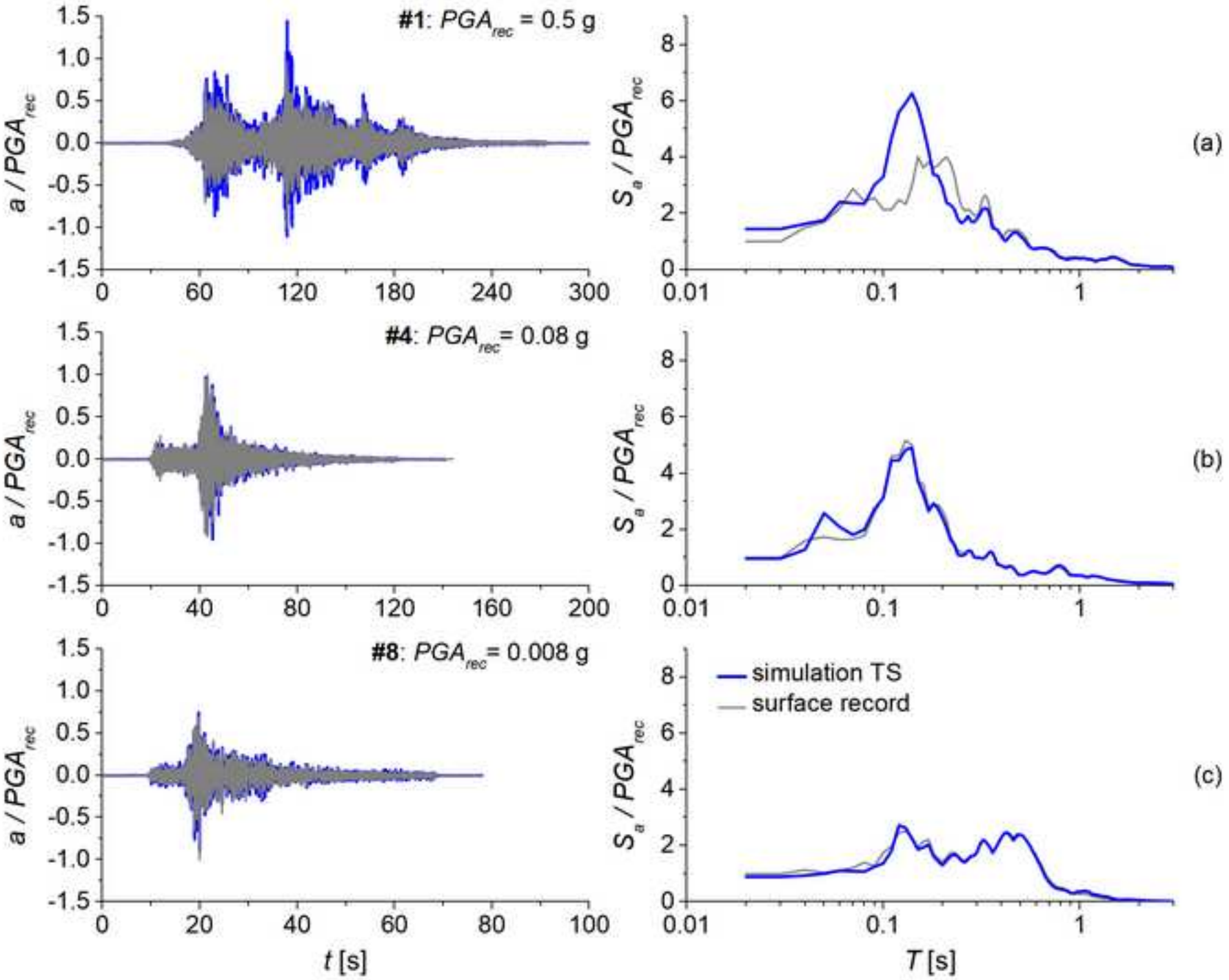

Figure_17
Click here to download high resolution image

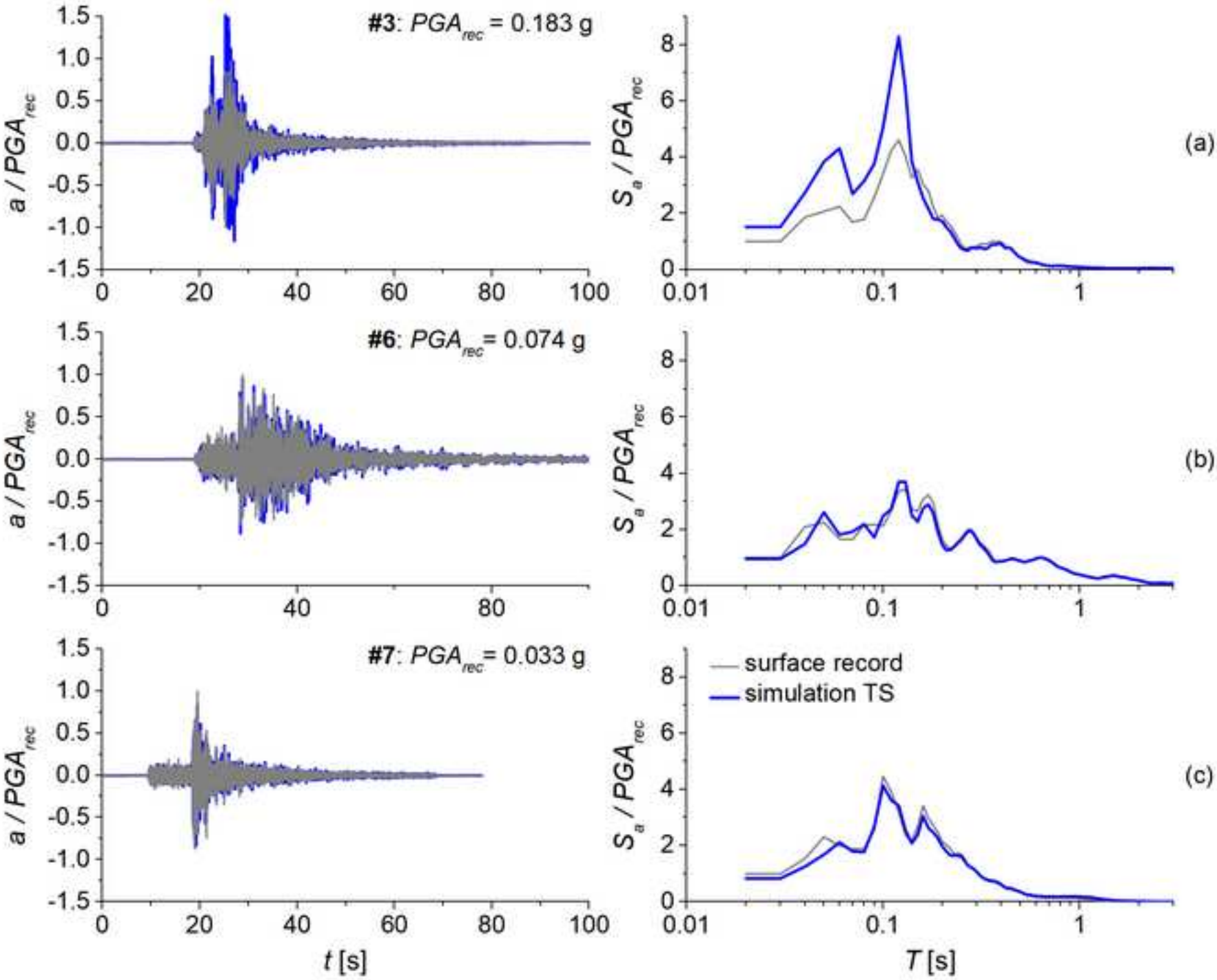

Figure_18
Click here to download high resolution image